

**AFRL-SN-WP-TR-2003-1111**

**ELECTRICALLY TUNABLE OPTICAL  
DELAY LINES**

**Dr. Thomas R. Nelson**

**Dr. John P. Loehr**

**Electron Devices Branch (AFRL/SNDD)**

**Aerospace Components and Subsystems Division**

**Sensors Directorate**

**Air Force Research Laboratory, Air Force Materiel Command**

**Wright-Patterson Air Force Base, OH 45433-7318**



**Dr. Joseph Van Nostrand**

**AFRL/MLPSM**

**Dr. Ralph E. Sherriff**

**AFRL/MLPA**

**APRIL 2003**

**Final Report for 01 October 1999 – 30 September 2002**

**Approved for public release; distribution is unlimited.**

**SENSORS DIRECTORATE**

**AIR FORCE RESEARCH LABORATORY**

**AIR FORCE MATERIEL COMMAND**


**WRIGHT-PATTERSON AIR FORCE BASE, OH 45433-7318**

## NOTICE

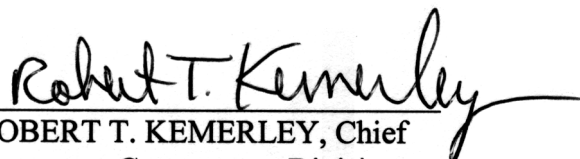
Using government drawings, specifications, or other data included in this document for any purpose other than government procurement does not in any way obligate the U.S. Government. The fact that the government formulated or supplied the drawings, specifications, or other data does not license the holder or any other person or corporation; or convey and rights or permission to manufacture, use, or sell any patented invention that may relate to them.

This report has been reviewed by the Office of Public Affairs (ASC/PA) and is releasable to the National Technical Information Service (NTIS). At NTIS, it will be available to the general public, including foreign nations.

This technical report has been reviewed and is approved for publication.

  
THOMAS R. NELSON, Project Engineer  
Electron Devices Branch  
Aerospace Components Division

  
KENICHI NAKANO, Chief  
Electron Devices Branch  
Aerospace Components Division

  
ROBERT T. KEMERLEY, Chief  
Aerospace Components Division  
Sensors Directorate

Copies of this report should not be returned unless return is required by security considerations, contractual obligations, or notice on a specific document.

<b>REPORT DOCUMENTATION PAGE</b>				<i>Form Approved</i> OMB No. 0704-0188				
The public reporting burden for this collection of information is estimated to average 1 hour per response, including the time for reviewing instructions, searching existing data sources, gathering and maintaining the data needed, and completing and reviewing the collection of information. Send comments regarding this burden estimate or any other aspect of this collection of information, including suggestions for reducing this burden, to Department of Defense, Washington Headquarters Services, Directorate for Information Operations and Reports (0704-0188), 1215 Jefferson Davis Highway, Suite 1204, Arlington, VA 22202-4302. Respondents should be aware that notwithstanding any other provision of law, no person shall be subject to any penalty for failing to comply with a collection of information if it does not display a currently valid OMB control number. <b>PLEASE DO NOT RETURN YOUR FORM TO THE ABOVE ADDRESS.</b>								
<b>1. REPORT DATE (DD-MM-YY)</b> April 2003		<b>2. REPORT TYPE</b> Final		<b>3. DATES COVERED (From - To)</b> 10/01/1999 – 09/30/2002				
<b>4. TITLE AND SUBTITLE</b> ELECTRICALLY TUNABLE OPTICAL DELAY LINES				<b>5a. CONTRACT NUMBER</b> In-house				
				<b>5b. GRANT NUMBER</b>				
				<b>5c. PROGRAM ELEMENT NUMBER</b> 61102F				
<b>6. AUTHOR(S)</b> Dr. Thomas R. Nelson and Dr. John P. Loehr (AFRL/SNDD) Dr. Joseph Van Nostrand (AFRL/MLPSM) Dr. Ralph E. Sherriff (AFRL/MLPA)				<b>5d. PROJECT NUMBER</b> 2305				
				<b>5e. TASK NUMBER</b> PN				
				<b>5f. WORK UNIT NUMBER</b> 01				
<b>7. PERFORMING ORGANIZATION NAME(S) AND ADDRESS(ES)</b> Electron Devices Branch (AFRL/SNDD) Aerospace Components and Subsystems Division Sensors Directorate Air Force Research Laboratory, Air Force Materiel Command Wright-Patterson Air Force Base, OH 45433-7318				<b>8. PERFORMING ORGANIZATION REPORT NUMBER</b> AFRL-SN-WP-TR-2003-1111				
<b>9. SPONSORING/MONITORING AGENCY NAME(S) AND ADDRESS(ES)</b> Sensors Directorate Air Force Research Laboratory Air Force Materiel Command Wright-Patterson AFB, OH 45433-7318				AFRL/MLPSM  AFRL/MLPA				
				<b>10. SPONSORING/MONITORING AGENCY ACRONYM(S)</b> AFRL/SNDD				
<b>11. SPONSORING/MONITORING AGENCY REPORT NUMBER(S)</b> AFRL-SN-WP-TR-2003-1111								
<b>12. DISTRIBUTION/AVAILABILITY STATEMENT</b> Approved for public release; distribution is unlimited.								
<b>13. SUPPLEMENTARY NOTES</b> Report contains color.								
<b>14. ABSTRACT</b> In this report, we detail the methodology and results for design, fabrication, and characterization of electrically tunable optical delay lines. Our approach focuses on monolithic semiconductor multilayer heterostructures (Distributed Bragg Reflector) to produce true time delays for incident transmitted optical pulses. Quantum wells are grown in every other layer of the DBR stack. When a field is applied across the device, the well-known Quantum Confined Stark Effect causes both absorption and refractive index changes in these layers. Changing the field changes the effective optical path length, thereby providing electrically tunable true time delays. In-house design, growth, and processing were all accomplished by AFRL. Simple broadband transmission characteristics were also performed in-house, while true-time delay experiments were performed exclusively by collaborators from the University of Alabama at Huntsville.								
<b>15. SUBJECT TERMS</b>								
<b>16. SECURITY CLASSIFICATION OF:</b> <table border="1" style="width: 100%; border-collapse: collapse;"> <tr> <td style="padding: 2px;"><b>a. REPORT</b> Unclassified</td> <td style="padding: 2px;"><b>b. ABSTRACT</b> Unclassified</td> <td style="padding: 2px;"><b>c. THIS PAGE</b> Unclassified</td> </tr> </table>			<b>a. REPORT</b> Unclassified	<b>b. ABSTRACT</b> Unclassified	<b>c. THIS PAGE</b> Unclassified	<b>17. LIMITATION OF ABSTRACT:</b> SAR		<b>18. NUMBER OF PAGES</b> 44
<b>a. REPORT</b> Unclassified	<b>b. ABSTRACT</b> Unclassified	<b>c. THIS PAGE</b> Unclassified						
<b>19a. NAME OF RESPONSIBLE PERSON (Monitor)</b> Thomas R. Nelson			<b>19b. TELEPHONE NUMBER (Include Area Code)</b> (937) 255-1874 x3361					

# LABORATORY RESEARCH INITIATION REQUEST (LRIR) FINAL REPORT

**Title:** Electrically tunable Optical Delay Lines

**Laboratory Task Managers:**

Dr. Thomas R. Nelson, Jr. (AFRL/SNDD; 08/00 – 12/02) Phone: (937) 255-1874 Ext. 3361

Dr. John P. Loehr (AFRL/SNDD; 01/99 – 08/00)

Dr. Joseph Van Nostrand (AFRL/MLPSM; 04/00 – 12/02) Phone: (937) 255-2227 Ext. 3389

Dr. Ralph E. Sherriff (AFRL/MLPA; 01/99 – 04/00)

**AFOSR Program Manager:** Dr. Gernot Pomrenke (AFOSR/NE) Phone: (703) 696-8426

**Research Objectives:**

- Investigate the design, growth, fabrication and testing of electrically tunable optical delay lines based on Quantum Well Distributed Bragg Reflectors (QWDBRs).
- Establish the practical limits of QWDBR delay lines for optical beam steering and image correction.
- Investigate the design, growth, fabrication, and testing of optical phased arrays using Vertical Cavity Surface Emitting Lasers with integrated QWDBR delay lines.

**Synopsis of Attempted Research:** When an optical pulse is transmitted through a Distributed Bragg reflector (DBR), it can experience delays of 10 or more cycles. This effect has already been demonstrated for 1.5-micron light. Unfortunately, DBR structures alone offer no way to tune the delay interval, apart from mechanical angle tuning. We proposed to create *electrically tunable* optical delay lines by introducing quantum wells into each period of the DBR. The excitonic resonance in each quantum well strongly influences the local index of refraction and the associated optical path length of the well. By applying an electric field across the quantum wells, we can shift the exciton peak via the quantum-confined Stark effect (QCSE). Thus, we can electrically tune the optical path length and associated optical delay in these Quantum Well Distributed Bragg Reflector (QWDBR) optical delay lines. Preliminary calculations (shown herein) indicated a potential tuning range of nearly 10 cycles for our modified structures.

Electrically tunable, multi-cycle optical delay lines have the potential to address the needs of several important space-based Air Force systems. Arrays of QWDBR delay lines could electrically steer optical beams or correct aberrated optical images. We could also fabricate an *optical phased array* by appending a tunable delay line to each element in an optical emitter array. These arrays would let Air Force system designers apply many radio-frequency techniques to optical systems.

QWDBR delay lines also present many interesting scientific and technological challenges. There are intrinsic trade-offs between delay time, pulse bandwidth, and optical transmission. Also, since high-power optical beams may ultimately be incident on these structures, the physics of excitonic absorption in the high-intensity regime is important. In particular, it is critical to determine how strongly the refractive index changes persist when photogenerated carriers act to screen the exciton. Finally, precision growth of heterostructures and quantum wells is critically important. Our calculations showed that the tuning range is strongly dependent on the sharpness of both the excitonic absorption resonance and the DBR transmission resonance.

In this report, we detail the methodology and results for design, fabrication, and characterization of electrically tunable optical delay lines based on this approach. In-house design, growth, and processing were all accomplished by AFRL. Simple broadband transmission characteristics were also performed in-house, while true-time delay experiments were performed exclusively by collaborators from the University of Alabama at Huntsville.

## I. Introduction

Electrically tunable optical delay lines would be an enabling technology for a wide variety of new Air Force systems. As stand-alone arrays, these devices could be used for beam steering and image correction in pre-existing beams. If integrated with an array of optical emitters, they could also produce an optical phased array, an important enabling technology for optical LADAR as well as potential use in several directed energy systems. Finally, tunable optical delays could also present a photonic means for true-time delay elements applied to traditional RF radar systems. Space-based systems, in particular, could profit from all of these capabilities. Such photonic components would experience no reaction forces, and free space optical interconnections or lightweight fiber optic connections may be utilized—both critical features for a space-based platform. In this final report, we detail a 3-year research effort that attempted to fabricate a monolithic semiconductor structure that functions as an electrically controllable optical delay line. Our device concept was based on proven and robust physical effects. Application of these effects to practical devices required a comprehensive scientific investigation of the underlying principles governing device operation. This proposal was given a high priority by the Sensors Directorate Chief Scientist, and was strongly supported by AFOSR program managers Alan Craig, Kent Miller, and Gernot Pomrenke.

Our approach was based on optical pulse delay in Distributed Bragg Reflectors (DBRs). These reflectors have traditionally been used for the formation of very high reflectivity mirrors ( $R > 99.999\%$ ) for use in vertical-cavity surface-emitting lasers (VCSELs). Previous researchers discovered, however, that an optical pulse passing through the transmission bandedges of a DBR experience a delay of 10 or more cycles [1]. This effect has also been demonstrated for 1.5-micron light, important for low-loss fiber optic transmission applications [2]. Unfortunately, DBR structures *alone* offer no way to tune the delay interval, apart from mechanical angle tuning [1]. Our methodology sought to develop a means to electrically tune the optical delay lines by introducing quantum wells into each period of the DBR, as shown in Fig. 1. The excitonic resonance in each quantum well strongly influences the local index of refraction and the associated optical path length of the well. By applying an electric field across the quantum wells, we can shift and broaden the exciton peak via the Quantum-Confined Stark Effect (QCSE). Thus, we can electrically tune the optical path length and associated optical delay. Our preliminary calculations showed that we would expect a tuning range of nearly 10 cycles for our modified structures.

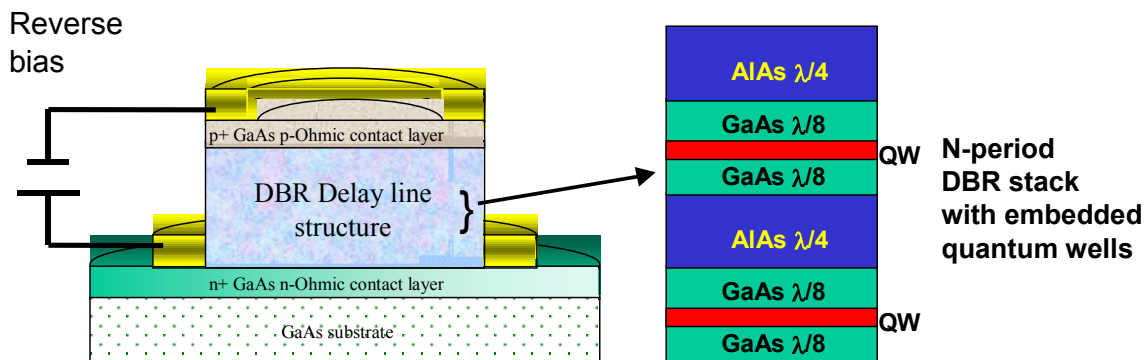


Figure 1 - Schematic depiction of the proposed device.

The devices detailed here were all grown by molecular beam epitaxy (MBE) by researchers from the Materials Directorate (James Ehret, Joseph Van Nostrand, or Xinghua Xie). Indeed, as the growth of such devices is every bit as difficult as a VCSEL (perhaps more so!), much of the time, effort, and capital for this project were devoted to precision materials growth. These advances and methods will be illustrated where appropriate. Researchers in the Sensors Directorate performed cleanroom fabrication of these structures. Both Directorates collaborated on the theory of these devices, and on bias-dependent CW optical testing. Extensive tests of optical pulse delay and transmission phase changes were performed by the research group of Prof. Richard Fork at the University of Alabama at Huntsville (UAH). All three members (SNDD, MLPA, and UAH) worked jointly to design and improve the performance of these structures as much as time and capital allowed.

In Section II we outline a few applications of these devices to important Air Force systems, and briefly overview the current state of the art on competing or complementary technologies. An overview background to our approach is presented in Section III. In Section IV we detail our growth, fabrication, and characterization efforts. Finally, Section V summarizes conclusions based upon our work, and gives suggestions for further study.

## **II. Air Force Relevance / Competing Methodologies**

There are several important air- and space-based Air Force systems that require electrically tunable, multi-cycle optical delays. For example, many space-based systems require free-space optical interconnects. Because of the large distances that separate the communication elements in these systems, tracking and pointing of the optical beams poses a critical technical barrier. Furthermore, mechanical pointing systems are often unacceptable because they disturb the satellite via reaction forces. Only electrical beam-steering elements may be used. By fabricating arrays of our delay lines and applying an increasing delay across the array, we could steer the beam electrically.

Optical delay line arrays could also be used for image correction. For example, beams reflected from the cheap deformable-membrane mirrors in space-based surveillance systems are likely to contain large aberrations. In these systems, holographic techniques can ascertain the mirror-induced aberration. This information could then be sent to an electrically tunable, spatially addressable delay line array at the image plane, which would correct the beam and recover the image.

The applications above dealt with steering or correcting pre-existing optical beams. Optical delay lines could also be used in systems that *create* coherent optical beams. By appending a tunable delay line to a Vertical-Cavity Surface-Emitting Laser (VCSEL), we can change the phase of the emitted beam. A closely spaced, independently addressable, two-dimensional array of these structures could have the phase of all the constituent beams tuned to produce a single coherent beam. Such *optical phased arrays* have long been a goal of Air Force system designers, and would allow many radio-frequency techniques to be translated into shorter-wavelength, higher-resolution, more covert optical systems.

An excellent review article by McManamon *et al.* [3] gives some insight into the development of beamsteering elements for optical phased array systems. While the work in that article focused on a phase-reset grating approach (i.e. not on a true-time delay principle), it nonetheless bears mentioning here as a reference point for comparison of our device concept relative to other approaches.

A “wish list” of qualities desirable for elements in an optical phased array system would include the following:

- High efficiency (both grating efficiency and low absorption/scattering)
- Large steering angles, meaning large time delays or phase shifts
- Low power, current, or voltage operation (especially true for space-based applications)
- An ability to handle large optical fluences
- Fast switching times (sub millisecond at minimum)
- Random access addressing (Field of Regard/Field of View)
- High precision/stability
- Avoid moving parts (especially for space-based applications)
- Avoid optical frequency shifts

One of the more common approaches toward generation of optical beamsteering devices is by means of the electro-optic effect. Indeed, 1-D phased arrays using bulk lithium tantalate [4] and lithium niobate [5] electro-optic prism deflector structures were demonstrated many years ago. These devices suffered from relatively small phase shifts under applied fields, making large devices ( $\sim$  millimeters) and large applied biases ( $\sim$  500 V) necessary in order to achieve any significant steering angles. More recently, use of the electro-optic effect in AlGaAs waveguides[6] has also been demonstrated. Here, microfabrication techniques allowed very small spacing between waveguides, which greatly reduced scattering of electromagnetic energy into grating sidelobes. Additionally, such field effects in these small-scale, semiconductor waveguide devices meant very fast access times (on the order of nanoseconds). However, only  $\pm 7.5$  mrad steering angles were achieved, making them inappropriate for any practical beamsteering applications.

Acousto-optic modulators have been used with a great deal of success [7] for many terrestrial applications. However, by their very nature, these devices introduce significant amounts of vibration to any system, making them unattractive candidate for any space-based application. Furthermore, the small path length changes again require nontrivial device sizes (cm-scales are common) to achieve significant steering angles, and there is an associated change in frequency (similar to a Doppler shift) that occurs in these structures. Indeed, the larger the path difference achieved, the more the frequency change from the fundamental.

Another method that has met with intense research enthusiasm has been the use of liquid crystal structures [3]. Here, one is limited to particular input polarizations due to the nature of the effect (optical path differences occurring along particular orientation axes of the crystals, giving rise to refractive index changes preferential to those axes). Nevertheless, the spacing between pixels in a liquid architecture can be made quite small, so as to approach the ideal  $\lambda/2$  center-to-center spacing. Such pitch in pixels greatly decreases side-lobe scattering. These devices operate on a millisecond timescale, suitable for many applications, but will suffer when operated at very low temperatures (viscosity effects in the supporting medium). Additionally, development of durable, highly conductive yet very low-loss transparent contacts remains an area of intense scrutiny for ultimate high-power applications such as phased array optical radar systems.

Researchers are also investigating other technology approaches, such as the use of micro-electro-mechanical systems (MEMS) to actuate zone plate microlenses [8], or use of piezo-electric

micro-actuated fiber “stretchers” to actually physically lengthen optical fiber cables to produce an optical path length change [9]. The MEMS approach can be configured to produce 2-D steering, but is somewhat bulky, and won’t allow a dense array of closely packed devices for a phased array application. The fiber stretcher approach also involves mechanical actuation, and will degrade over long periods of time, especially if the fibers are thermally cycled in operation.

### III. Electrically Tunable QWDBR Approach

A Distributed Bragg Reflector (DBR) is a multilayer structure that relies on the constructive interference of multiple reflections to achieve very high reflectivity at particular design wavelengths. At other wavelengths, the interference produces a number of characteristic features in the DBR transmission spectrum. Figure 2 shows the transmission spectrum for a 28-period GaAs/AlAs DBR grown in-house. The wide region of low transmission is usually referred to as the mirror’s transmission stop band. We will refer to the two transmission peaks that bracket the stop band as the DBR transmission resonances or, in analogy to semiconductor bandstructure theory, as the optical bandedges, denoted  $\lambda_+$  and  $\lambda_-$  for the long- and short-wavelength resonances, respectively.

Bendickson *et al.* originally proposed pulse group delays in DBR structures [1]. They predicted that pulses at the transmission resonance wavelengths would experience a delay that is proportional to the square of the number of DBR periods. A research group that included our collaborator, Dr. Richard Fork, demonstrated this effect experimentally at a wavelength of 1.529  $\mu\text{m}$  [2]. Optical pulse delays of 0.27 ps were obtained with a 30-period GaAs/AlAs DBR. This corresponds to a phase change of approximately 52 cycles compared to propagation through the same thickness of bulk GaAs. For their experimental conditions (ps-scale pulse durations), pulse distortion was negligible. The results agreed with calculations based on both pulse propagation simulations [2] and frequency-domain techniques [1]. The major drawback of the simple DBR structure is that the delay can only be adjusted by changing the incident angle of the pulse. Such mechanical tuning is undesirable for many systems applications.

DBR delay lines would be more powerful and flexible devices if the delay could be tuned electrically. This can be achieved by electrically altering the refractive index of some or all of the DBR layers, or by changing the physical thickness of one or more layers in some fashion. By placing quantum wells inside the DBR, we can use the quantum confined Stark effect (QCSE) to obtain index changes that are large enough to effect the delay. QCSE occurs when an electric field is applied perpendicular to the plane of the well. The field red shifts and broadens the absorption spectrum of the excitons in the well [10]. Changes in absorption cause changes in the refractive index in accordance with the Kramers-Kronig transformation. Unlike some non-linear optical effects in semiconductors, QCSE is strong at room temperature and high electric fields, making it a practical effect for device applications. Additionally, as this is a field effect, and not a thermal, current, or carrier based effect, the times scales involved are extremely short (order of picoseconds), making this an inherently fast device concept.



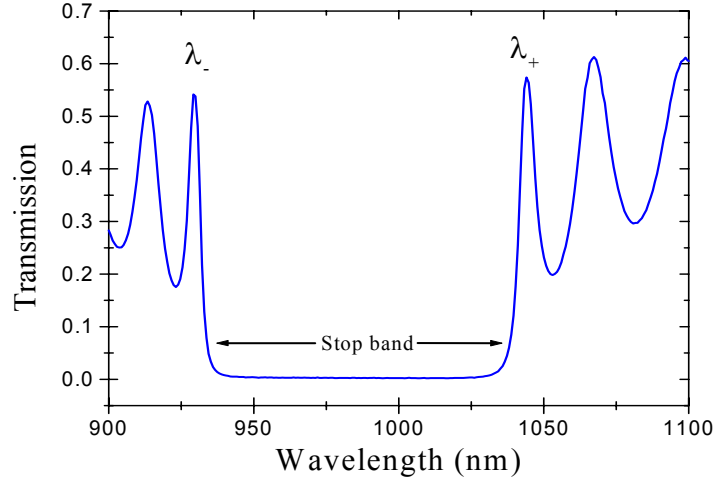


Figure 2 - Transmission spectrum of a 28-period GaAs/AlAs DBR stack grown in-house by MBE. Here,  $\lambda_-$  and  $\lambda_+$  label the short- and long-wavelength transmission resonances, respectively.

The use of quantum wells and the QCSE for electric field control of DBR optical properties has already been demonstrated. Blum *et al.* [11] were interested in electrically tuning the Fabry-Pérot cavity resonance in a surface-emitting laser to the peak of the gain medium. They pointed out that this could be achieved by tuning the reflectance phase of one or both of the mirrors that comprise the resonator. To fashion a tunable mirror, they added InGaAs wells to an InGaAs/InP DBR. Bias across the mirror altered the reflectance phase via QCSE. For a 31-period mirror, with every other layer containing 8 quantum wells, they found differential changes in transmission of 14% at 1570 nm for an applied reverse bias of 17 V. In a later paper [12], an interdigitated contact scheme produced similar index changes at lower drive voltages. In this case, 5 InGaAs wells were grown in each GaAs high index layer of a 20-period GaAs/AlAs DBR mirror. The center of the mirror stop band was at 1033 nm, while the exciton peak absorption for zero applied bias was near 980 nm. They observed reflectivity changes as large as 12% for application of only +1 V bias.

To demonstrate that our proposed structure could generate sufficient delays for practical use, we performed a series of initial “proof-of-concept” simulations. The quantum well refractive index and absorption were simulated as Lorentzian oscillators for simplicity. The linewidth and peak absorption were chosen to be consistent with the absorption spectra of in-house grown InGaAs quantum wells. The absorption peak was placed near 945 nm. To simulate the effect of an applied field on the absorption, we shift the Lorentzian peak by  $-23$  meV and double the linewidth while halving the peak absorption (conservation of oscillator strength). These numbers are consistent with achievable QCSE results in the literature [13,14]. Figure 3 displays the model extinction coefficient and refractive index for both the unbiased and biased quantum well.

To get numerical results, we must choose a design wavelength. However, there exists an inherent tradeoff between absorption losses and achievable changes in refractive index when choosing the design wavelength for the DBR delay line. The index change is largest at the peak of the unbiased exciton absorption. How close we may operate to this exciton resonance will be determined by the amount of acceptable absorption loss through the device.

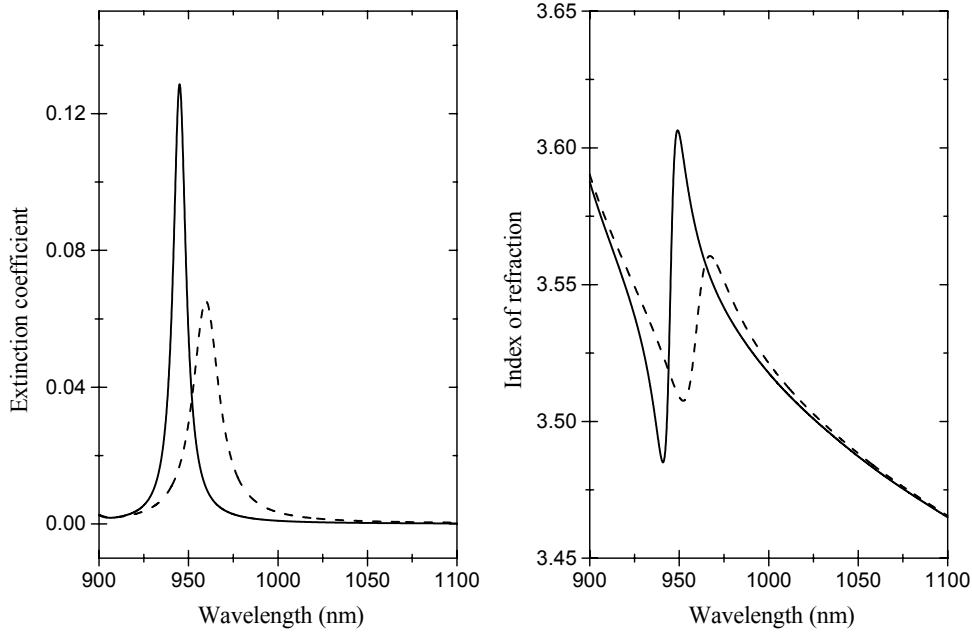


Figure 3 - Lorentzian oscillator model of the quantum-well extinction coefficient and refractive index without (solid) and with (dashed) applied field. To simulate the effects of reverse bias, we assume a red shift of 23 meV and a broadening and peak absorption reduction factor of 2.

The design of these QWDBR delay line structures is further complicated by how electric fields localize in these structures, and how much “real estate” is available, that is, the constraints on individual layer thicknesses that must be maintained to achieve successful operation. Figure 4 is a transfer-matrix simulation demonstrating that the square of the electric field amplitude,  $|E|^2$ , at the two possible design wavelengths in the structure modeled in Figure 2. One sees that at  $\lambda_-$  the electric field localizes in the lower refractive index layers of the structure, while for  $\lambda_+$ , the case is the opposite, and the field maximizes in the high refractive index layers. This turns out to be very beneficial for the designs we ultimately implemented. Leveraging our prior expertise in VCSEL growth, we sought to utilize InGaAs quantum wells with GaAs barriers and an applied external potential to produce QCSE index shifts in these layers. Our designs make use of the  $\lambda_+$  resonance, which naturally has a strong interaction with the electric field. Indeed, these simulations show that there is a factor of 8.5X resonant enhancement of  $|E|^2$  in the central GaAs layers, similar to standing wave patterns generated in a Fabry-Perot cavity.

For the sake of modeling, we initially chose a design wavelength of 1040 nm. The DBR mirror stacks were designed to place the long-wavelength transmission resonance at this wavelength. The Lorentzian lineshapes (see Figure 3) for biased and unbiased absorption have a refractive index difference of  $\Delta n = -.0013$  at this wavelength.

The modeled phase change is seen to increase approximately quadratically with  $N$ , similar to the findings of Bendickson *et al.* [1]. A rough measure of the pulse bandwidth that can be transmitted without significant distortion is the full-width half-maximum (FWHM) of the DBR

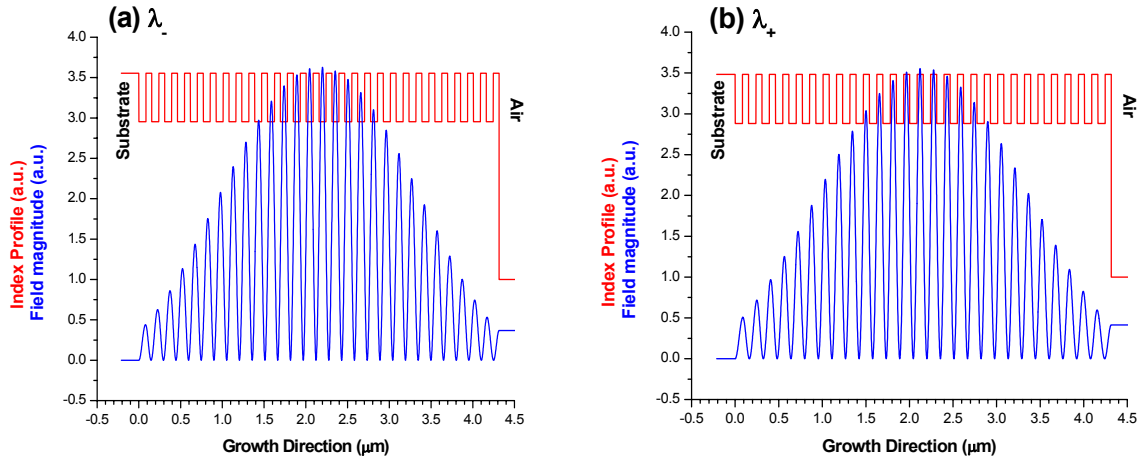


Figure 4 - Simulation of  $|E|^2$  localization for (a)  $\lambda_-$ , with localization in the low-index AlAs layers, and (b)  $\lambda_+$ , with localization in the high-index GaAs layers, for the structure given in Figure 2.

transmission resonance. As Fig. 5 shows, the FWHM decreases nearly quadratically with the number of periods. The figure clearly demonstrates that there will be a tradeoff between achievable delay and pulse bandwidth. As a point of reference, a transform-limited Gaussian pulse that is 10 ps in duration and centered at 1.0  $\mu\text{m}$  would have a wavelength bandwidth of 0.15 nm, whereas a 10-fs pulse would have a bandwidth of 150 nm. This illustrates that one must plan in advance the pulse shape and duration to be used in this proposed delay line structure, as the bandedge resonances rapidly become too short to support non-distorted ultrashort pulses.

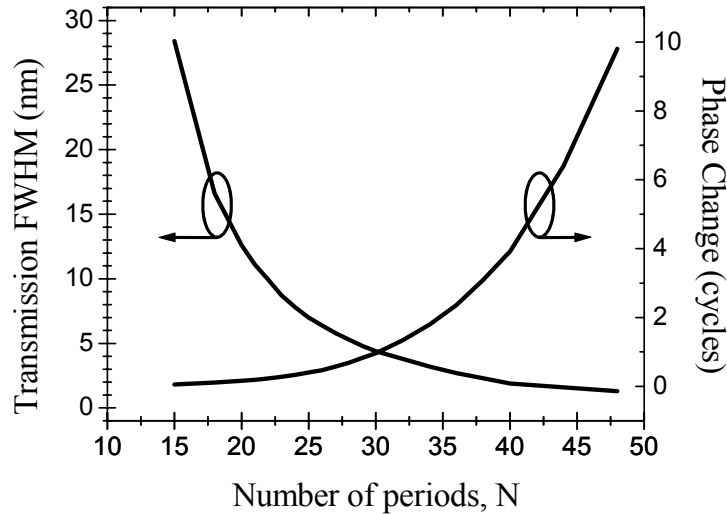


Figure 5 - Simulation results showing an increase in phase change (modulo  $2\pi$ ) and decrease in transmission FWHM with increasing number of DBR periods.

#### IV. In-house Results: Growth, Fabrication, and Characterization

Successful development of electrically tunable DBR delay lines requires precise material growth and sophisticated device fabrication capabilities. For this effort, we leveraged much of our history in the arena of successful growth and fabrication of vertical-cavity surface-emitting lasers (VCSELs) to yield AFRL's first ever demonstration of a tunable optical delay line device. The total amount of *tunable* time delay was much less than anticipated, however, and in Section V we'll present explanations for this behavior.

The Materials Directorate at AFRL (AFRL/MLPSM) has successfully grown accurate DBR structures for VCSEL applications at several wavelengths. Accurate and reproducible growth of DBRs relies on several state-of-the-art in-situ monitors that MLPSM and SNDD have jointly implemented on the MLPSM *Varian GEN II* MBE machine. For example, reflection high-energy electron diffraction (RHEED) measurements are a common method used to extract material growth rates. Our RHEED oscillation system was dramatically improved using a more sensitive detection scheme. This allows a more accurate determination of GaAs growth rates, which translates directly into more accurate layer thicknesses during DBR growth. Further, during the course of this research, SNDD added a quasi-in-situ reflectometer system to measure the spectrum at various points in the growth cycle. This system mounts to an optical port in the sample preparation/transfer chamber. Using a fitting program developed in-house, we can fit the reflectivity spectrum and extract both the GaAs and AlAs growth rates without having to break ultra-high-vacuum and remove the sample from the MBE system entirely. This dramatically reduces calibration turn-around times. In addition, both directorates teamed to purchase a carbon doping system for this MBE machine. Carbon allows us to grow our p+ contact layers with higher doping levels (see Figure 6). Higher doping permits achievement of applied fields that are transversely uniform. Further, carbon diffuses less than other dopants making carbon-doped heterostructures less sensitive to high temperatures during growth or fabrication.

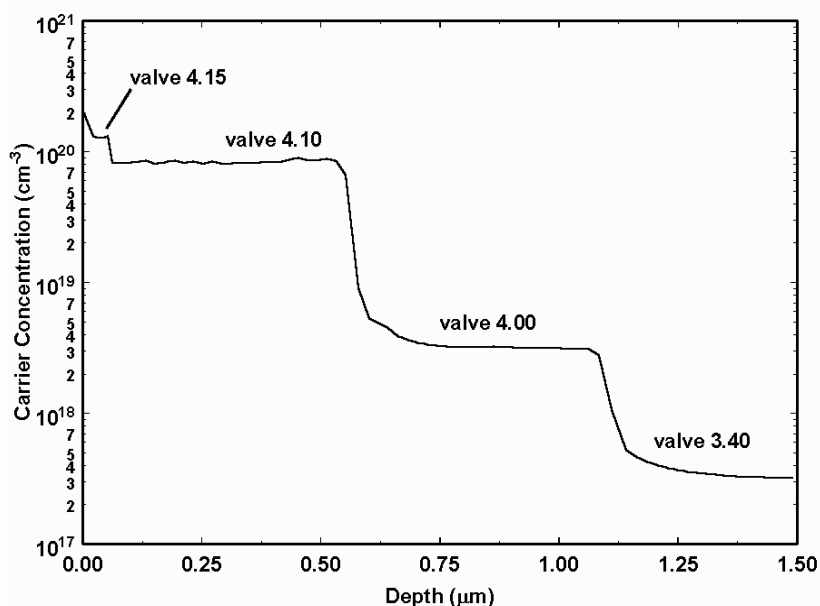


Figure 6 - Poloron measurement of effective carrier concentrations as a function of valve position for our CBr<sub>4</sub> doping system.

Finally, we also purchased components and developed an in-situ photoluminescence system for the MBE system. This last piece of the puzzle allows us to more accurately calibrate the growth of InGaAs/GaAs quantum wells used in the QWDBR devices. Indeed, we developed a growth methodology and fitting algorithm whereby we grow multiple quantum well structures, fit the multi-peaked PL spectrum, and extract the indium mole fractions from these fits. The methodology utilizes strain-inclusive bandstructure parameters obtained from a collaboration with Professor L.R. Ram-Mohan (Worcester Polytechnic Institute) based on an 8-band  $k \cdot p$  finite element method algorithm [15]. Figure 7 demonstrates the MLPSM growth of a sample with 12  $\text{In}_{0.18}\text{Ga}_{0.82}\text{As}$  quantum wells of thickness 80 Å separated by 1000 Å GaAs barriers. The high quality of growth is evident from the narrow absorption linewidth (6.65 nm = 8.1 meV) and high peak absorption (2.4 per micron) *at room temperature*.

The reason these improvements for MBE growth were critical for further development of the QWDBR delay line structures is that we must accurately position the absorption peaks of the wells relative to the DBR bandedge resonances. If the QWs have their absorption peak too close to  $\lambda_+$ , then Stark red shifts under applied field will result in the exciton peak shifting to  $\lambda_+$ , and pulses incident at this wavelength will experience strong attenuation. If the wells are placed shorter in wavelength (closer to  $\lambda_-$ ), then there will be no significant change in refractive index at  $\lambda_+$  to create an optical path length change, therefore no time delay tuning will occur.

The first step toward fabrication of a QWDBR delay line device was verification of suitable multiple quantum well growth, and then characterization of QCSE changes under applied fields. For this work, we grew a sample of twelve  $\sim 80$  Å  $\text{In}(x)\text{Ga}(1-x)\text{As}$  quantum wells with 1000 Å GaAs barriers (i.e., uncoupled, isolated quantum wells). The sample also had an  $n^+$  ( $1 \times 10^{18} \text{ cm}^{-3}$ ) substrate side and  $p^+$  ( $5 \times 10^{18} \text{ cm}^{-3}$ ) top contact layers. Such strained layer QWs have the advantage of having their primary radiative exciton transition (e1-hh1) wavelength near 980 nm, sufficiently below the bulk GaAs substrate bandedge (870 nm) to

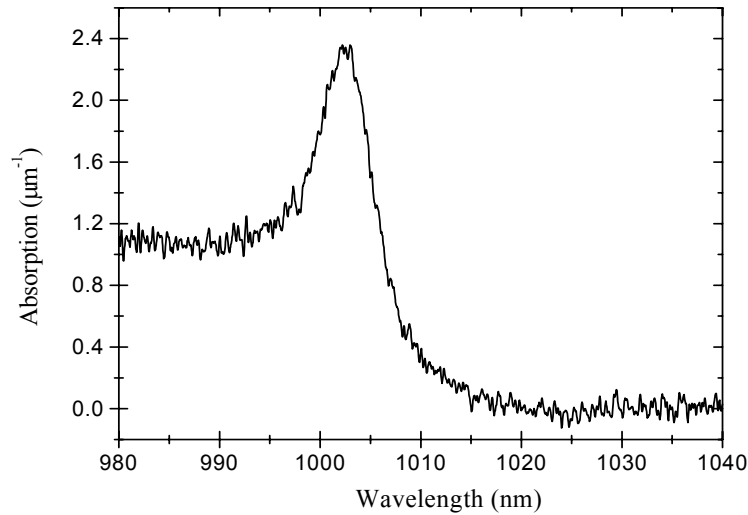


Figure 7 - Absorption spectrum for a sample of twelve 80-Å  $\text{In}_{0.18}\text{Ga}_{0.82}\text{As}$  quantum wells with 1000-Å GaAs barriers at room temperature.

allow transmission measurements to be performed at room temperature without the need for substrate thinning.

We generated a mask set for fabrication of QWDBR devices and applied our processing first to the MQW sample of Figure 7. There are only 3 cleanroom processing steps for such a device: Top p+ Ohmic contacts application (lift-off procedure); Mesa isolation etch via inductively coupled plasma reactive ion etching (ICP/RIE); and bottom n+ contact layer (lift-off). Devices were designed to be approximately 250  $\mu\text{m}$  in clear field opening to allow simple coupling of a fiber based white light source for reflection and transmission characterization of the samples. The top p-Ohmic contact layer consisted of nominally 500  $\text{\AA}$  Ti/2000  $\text{\AA}$  Au Ohmic metals evaporated on the top epitaxial surface of the wafer. We utilized ICP/RIE etching using a Unaxis 770 ICP/RIE system utilizing  $\text{Cl}_2/\text{BCl}_3$  etch chemistries. Since only quarters of a 3" diameter wafer were processed at any given time, the etching of this wafer in a loadlock system was done utilizing a 3" or 4" sapphire carriers for the MQW samples. We soft mounted the samples to these carriers using small amounts of chemically inert diffusion pump oil as a thermal contact "adhesive". We also developed an etch monitoring system to track etch depth as a function of etch time. Figure 8 shows a DBR sample we etched by this process, and also a plot of the reflection signal obtained during the etch. The final cleanroom-processing step was application of an n-Ohmic contact layer to the lower, etched surface of the sample. This allows application of reverse bias across the device to test the amount of quantum-confined Stark effect shifting and broadening of the e1-hh1 exciton absorption resonance depicted in Figure 7. We accomplished n-metal contacts through evaporation of 50  $\text{\AA}$  Ni / 170  $\text{\AA}$  Ge / 330  $\text{\AA}$  Au / 150  $\text{\AA}$  Ni / 3000  $\text{\AA}$  Au onto this lower surface.

In order to test the MQW devices, we had to develop both a characterization test bed and a means of packaging the devices such that they could be examined in transmission under bias. We were surprised to learn that very few commercially available electronics packages exist that have optically transparent openings for backside transmission of light. At the time of this investigation, we could only obtain such packages in bulk quantities (100 items minimum). In order to overcome this difficulty, we used an in-house micro-milling tool to generate our own package structures. This tool utilizes an x-y-z stepper control and extremely small milling bits to form patterns in various materials, including printed circuit boards, brass, copper, alumina,

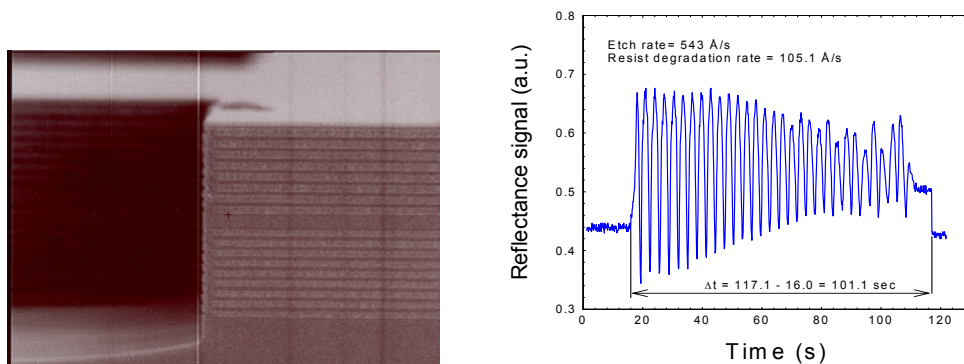


Figure 8 - Left: SEM Image of a DBR sample etched in the ICP/RIE system. Right: Time trace for reflectance monitoring of the etch for this sample.

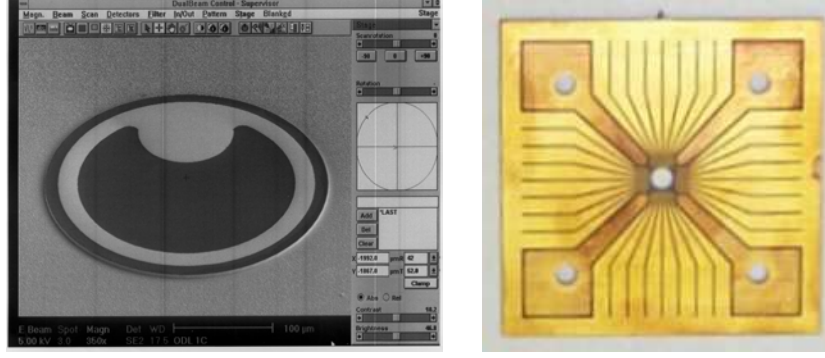


Figure 9 - Left: SEM image of a final fabricated QWDBR Optical Delay Line device. Right: Image of the transmissive micro-milled package created in-house for ODL characterization. This package designed for 8x8 arrays of ODL devices.

and aluminum. We applied this process to standard printed circuit board stock, and used a CAD tool to generate and transfer the package design geometry to the board. Figure 9 shows an image of a final fabricated device (end of cleanroom processing phase), as well as such a device placed into our in-house transmissive package.

For optical characterization of the QCSE, we used a white-light fiber probe source, and performed 1-to-1 imaging onto a sample to measure the dispersive transmission changes in the MQW sample under applied bias. All of these measurements were performed at room temperature, and utilized low intensity broadband illumination. To reduce the effects of above bandgap illumination degrading the QCSE, we placed a long-wave bandpass filter ( $\lambda_{\text{cut-on}} \approx 780 \text{ nm}$ ) between the light source and the MQW sample. To improve the signal-to-noise ratio in the experiment, lock-in detection methods were used. A schematic of the experimental setup is shown in Figure 10.

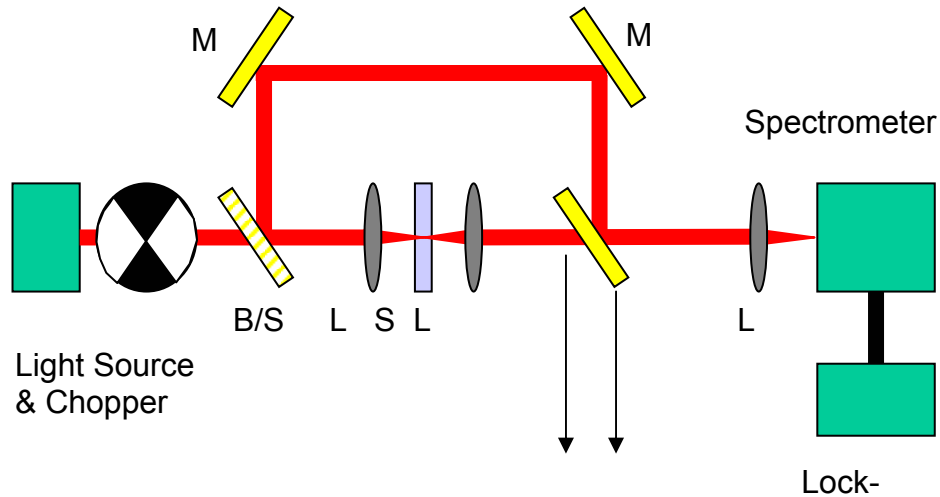


Figure 10 - Schematic of the characterization system for measuring differential absorption, transmission, and reflection for studying the QCSE in MQW and QWDBR samples.

Our reasons for setting up and performing measurements with this experimental arrangement were twofold. First, we wished to verify in general terms the performance of our quantum wells under bias, that is, notionally verify the amount of red shifting and broadening of our main exciton absorption peak as a function of applied field. We would first compare our results with those in the literature to determine not only the growth quality of our MQWs, but also verify the processing, packaging, and characterization capability at our disposal. This was intended to establish rough limits of the use of the QCSE for application in a tunable QWDBR ODL structure. Secondly, we hoped that such measurements would lead to a more careful and quantitative evaluation of the differential absorption change under applied reverse bias which could enable a cleaner calculation of the expected QWDBR ODL performance, as opposed to the simplified approach using the Lorentzian oscillator model discussed previously.

Our procedure began by performing differential absorption measurements on the multi-well sample as a function of applied bias. The differential absorption can be found from the measured differential transmission spectrum in the following way. First, ignoring the effects of reflection, determine the absorption in the sample from the relation  $\alpha(\omega)L = \ln[I_0(\omega)/I_T(\omega)]$ , or  $\alpha = -\ln[T]/L$ , that is, the absorption per unit length in the sample,  $\alpha(\omega)$ , is the negative of the natural log of the transmission coefficient of the sample,  $T$ , divided by the length or thickness of the sample,  $L$ . Here  $I_0(\omega)$  and  $I_T(\omega)$  are the experimentally measured transmission intensities of light without and with the sample, respectively. Under these assumptions, then, we may determine the differential absorption of **just** the quantum wells by subtracting the bulk dispersive absorption of the substrate, namely  $\Delta\alpha_{QW}(\omega) = \alpha_{QW}(\omega) - \alpha_{GaAs}(\omega)$ . To obtain the refractive index changes, we can “locally” apply the Kramers-Kronig relations. In principle, one must truly know the absorption spectrum over all frequencies or energies to obtain the refractive index. In practice, however, a good approximation can be made near the region of the exciton resonance,  $\omega_X - \Delta\omega < \omega < \omega_X + \Delta\omega$ , if the differential contribution to the total absorption outside of this region is negligible, i.e.  $\Delta\alpha_{QW}(\omega) \ll \alpha_{QW}(\omega)$ . In our case, the resultant quantum well refractive index is given by:

$$n_{QW}(\omega) = n_{GaAs}(\omega) + \frac{c}{\pi} \text{Pr} \int_{\omega-\Delta\omega}^{\omega+\Delta\omega} \frac{\Delta\alpha_{QW}(\omega')}{\omega'^2 - \omega^2} d\omega'$$

Here, Pr indicates the principle value of the integral is to be taken, and we’re making the assumption that the background index of refraction is that of gallium arsenide,  $n_{GaAs}$ , as a reasonable approximation for the low-mole fraction, strained (lattice-matched to GaAs substrate) quantum well material.

Our QCSE measurement results for this sample are illustrated in Figure 11. As expected, we found a significant amount of red shift of this resonance that followed an approximately quadratic dependence upon the applied bias, similar to results in previous publications. Despite the qualitatively good agreement between these results and those from previous researchers, we were not able to utilize these results for a quantitative analysis of the index change behavior. This is due to a number of factors. First, the background absorption due to the GaAs substrate and the GaAs buffer layer was not easily separated out. In previous works done at low temperature [16], one can “freeze out” much of the thermal broadening



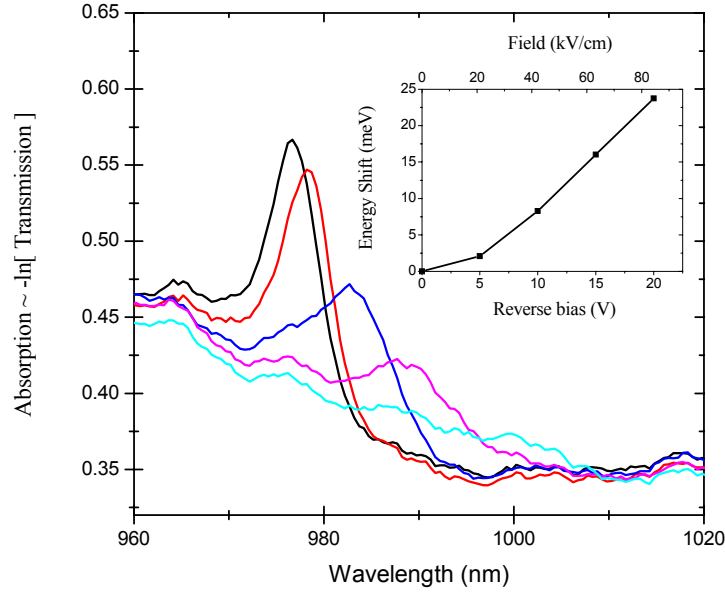


Figure 11 - Absorption measurements detailing the quantum-confined Stark effect for the MQW sample depicted in Figure 7. The inset shows the exciton peak energy shift as a function of applied field.

of the bulk GaAs bandedge absorption and more cleanly determine absorption due to just the quantum wells. Here, these effects are not easily separated. Furthermore, specular reflections from the back surface of the sample also give rise to long period interference fringes that further distort the system. One method to overcome such issues is to apply top and bottom surface anti-reflection coatings to remove these effects. From a cost-effectiveness standpoint, however, we felt that this was not an avenue worth pursuing. Given the qualitative agreement of our results to prior findings, we deemed it more appropriate to proceed with growth and fabrication of true QWDBR ODL samples rather than strive very hard to achieve numerical accuracy with this sample. Indeed, there is no guarantee that the results from a MQW sample would directly apply to the QWDBR ODL growth, and we felt it best to devote our time to process development of this, the desired structure.

We determined that the best design opportunity would be to target a structure that incorporated 3 QWs per GaAs high-index layer in the QWDBR structure. Indeed, this would be the maximum allowed for maintaining an effective quarter-wave layer standpoint and still maintain isolated (minimum 100 Å GaAs barriers) quantum wells. We also chose to target a device that, based on the simulations of Figure 5, would yield a time delay equivalent to 2 full cycles. This meant a structure with a number of periods  $N \geq 28$ . Our initial attempt at growth of this structure was tried on a Varian Gen “1.5” (modified Gen 1) system, as the Varian Gen 2 was down for repairs and bake-out. This system had yielded quantum wells of similar caliber to those of the Gen 2 system, and had also demonstrated the ability to grow DBR mirror layers (see Figure 12), but lacked the quasi-in-situ calibration tools of the Gen 2. In addition, this system possessed smaller effusion cells, meaning slightly less stable material fluxes, giving

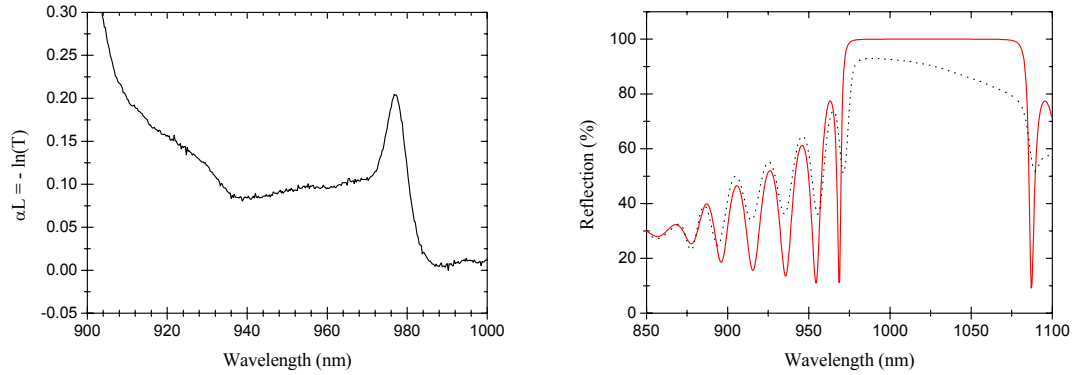


Figure 12 - Left: Measurement of the absorption,  $\alpha(\lambda)L$ , of a sample of 12 In(0.20)Ga(0.80)As quantum wells grown on the Gen 1.5 MBE system. Right: Reflectivity spectrum (dashed) of a 30-period DBR sample grown on the same system. The solid red curve is a fit to the measured data. The trail off in the reflectivity spectrum beyond 1.0  $\mu\text{m}$  is an artifact of the in-situ system, which has since been corrected.

rise to potential long-term drift in the growth rates. Nevertheless, in our attempt to make progress rapidly, we decided to use this growth system for a first attempt at a true QWDBR sample.

The first attempted QWDBR-ODL structure occurred in the Gen 1.5 system. This sample, denoted G1.5-1410, consisted of 30 periods of GaAs/AlAs DBR layers, designed to put the long-wavelength bandedge,  $\lambda_+$ , near 1064 (i.e. a center stopband design wavelength of  $\sim 1001$  nm). This wavelength was chosen due to its relevance to Nd:YAG laser applications. In each GaAs layer of the structure were 3 nominally 65-Å In(0.2)Ga(0.8)As quantum wells for QCSE tuning of the delay. The structure was grown on an undoped GaAs substrate to minimize absorption for our transmission experiments. A silicon doped GaAs buffer layer, nominally 2  $\mu\text{m}$  thick with carrier concentrations near  $2\text{e}+18 \text{ cm}^{-3}$  was grown prior to the device layers for n-metal contacting, and the last GaAs top layer was grown with Be doping ( $p^+ \sim 2\text{e}+18$ ) and no quantum wells for the top p-metal contact. Figure 13 shows both reflectivity and transmission spectra from this sample under a zero bias condition. The exciton absorption dip apparent from reflections and subsequent absorption in the first few layers is not very prominent, and is broad in comparison with the absorption spectrum of the MQW sample. This indicates that the interface quality (inhomogeneous well width broadening and peak absorption reduction) was significant.

In order to examine static effects (reflection or transmission changes) in this sample, it was necessary to perform the same cleanroom fabrication as was performed on the MQW QCSE sample of Figure 11. This again involved lift-off processing of top Ohmic contacts, mesa isolation etches, and a backplane n-metal Ohmic contact. In comparison to traditional VCSEL or DBR processing, the QWDBR-ODL samples possess much higher overall indium content. Indeed, the presence of 3 In<sub>x</sub>Ga<sub>1-x</sub>As quantum wells per period, with 29 such well containing periods, gives rise to more wells than even our MQW sample (87 versus 12 wells). As these wells are very thin—on the order of 100 Å or thinner—it was assumed that all of our previous process development would still be applicable. Unfortunately, this did not turn out to be the case with the ICP/RIE mesa isolation etch step. We found that the increased presence of

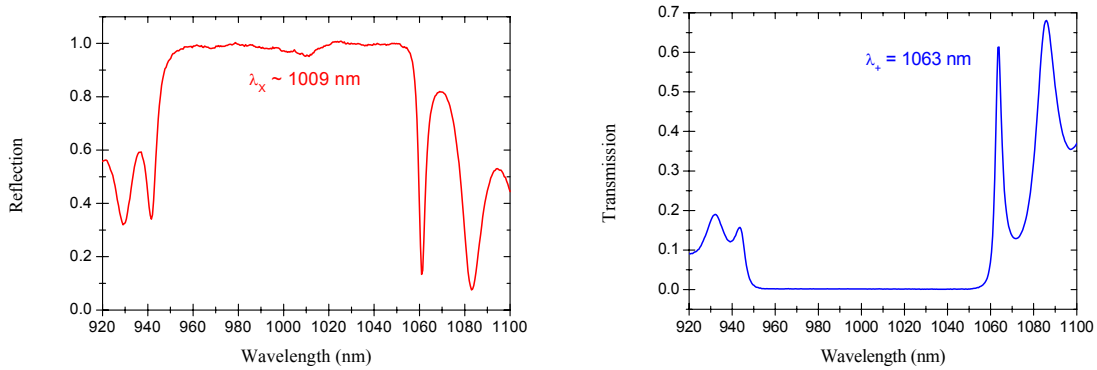


Figure 13 - Right: Reflection spectrum of first QWDBR growth, with exciton resonance at  $\sim 1009$  nm.

Left: Transmission spectrum of same sample under zero bias, show bandedge resonance at 1063 nm.

indium would inhibit the etch process. The low-temperature results performed initially showed sample roughness, and etch pits on the surface and on the sidewalls of the mesas. In some extreme cases, the etching would stop altogether, and we could actually watch this process degrade in real time using our etch reflectance monitoring system (see Figure 14).

It had been reported by the manufacturer of our etching system that a methane based etch chemistry worked very well for removing and patterning InGaAs materials [17]. Unfortunately, we had no additional mass flow controller capability, or even gas cabinet space, to accommodate this process. It took us several weeks of process development to determine a suitable solution to this problem. In the end, we found that simply using a higher wafer backside temperature during the etch process was suitable to liberate indium from the wafer using our standard etch chemistry. We had sufficiently good results raising the temperature from nominally 20 C (our standard VCSEL or DBR process temperature) to 70 C for these QWDBR-ODL samples. Accordingly, we were forced to investigate alternative photoresist masks for this process. The traditional 1800 Series of resists from MicroPosit proved insufficient, as they have a reflow temperature of  $\sim 90$  C, and would not stand up to both the backside 70 C heating in addition to the elevated temperature the sample surface sees while in the plasma. We found PMGI or  $\text{Si}_3\text{N}_4$  mask material to be of sufficient durability and practicality for this etch. Both PECVD and sputtered  $\text{Si}_3\text{N}_4$  dielectric depositions proved successful for this process. Figure 15 shows an SEM photograph (with ion beam milled cross section) of the improvements achieved through this new process on our QWDBR-ODL samples.

After the first generation QWDBR-ODL sample was processed and mounted into the aforementioned transmission package, wire bonds were attached, and the sample was measured in both reflection and transmission under applied reverse bias. The goal was to witness any sort of change at the long wavelength bandedge near 1064 nm due to QCSE effects in the wells. Figure 16 shows reflectivity spectra localized around the exciton peak and  $\lambda_+$  bandedge resonance in the search for any obvious changes. As anticipated, there is negligible influence on these spectra from application of an electric field as a result of the weak exciton absorption peak. Although this sample was used for process development, it was not sent to our collaborators at the University of Alabama in Huntsville for true-time delay measurement.

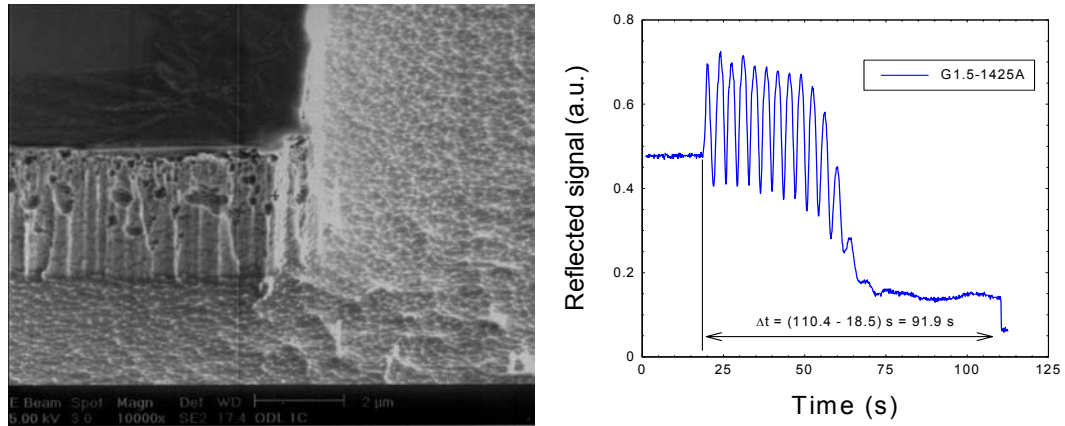


Figure 14 - Left: SEM image of our original ICP/RIE etch recipe applied to an QWDBR-ODL sample. The much higher indium content resulted in poor liberation and very rough etching characteristics. Right: Reflectance versus etch time for this recipe. The dramatic loss in reflectance oscillations indicated roughening of the surface and actual inhibition of the etching process.

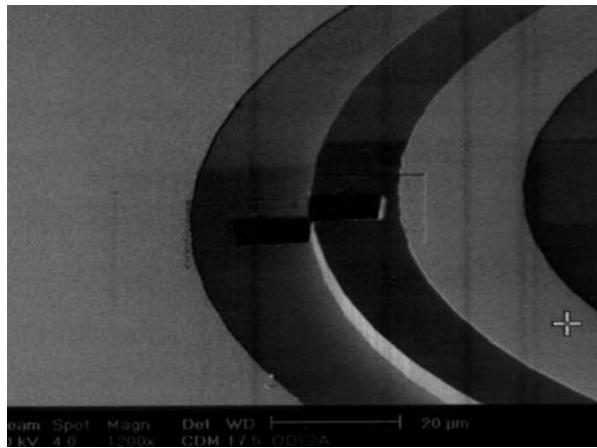


Figure 15 - SEM Micrograph of the improved etch process run on a QW-DBR ODL sample.

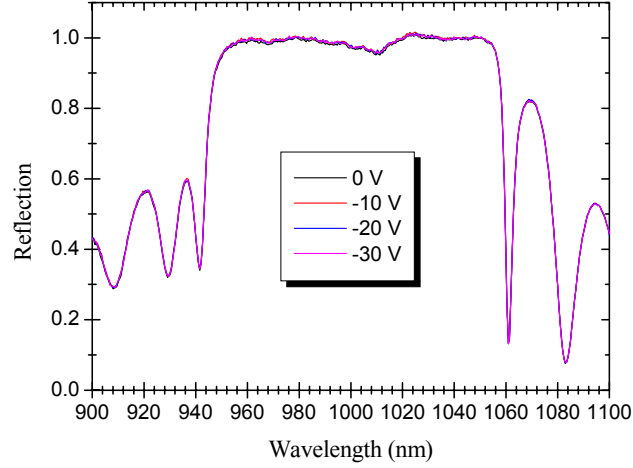


Figure 16 - Reflection spectra for first generation QWDBR-ODL sample under applied bias.

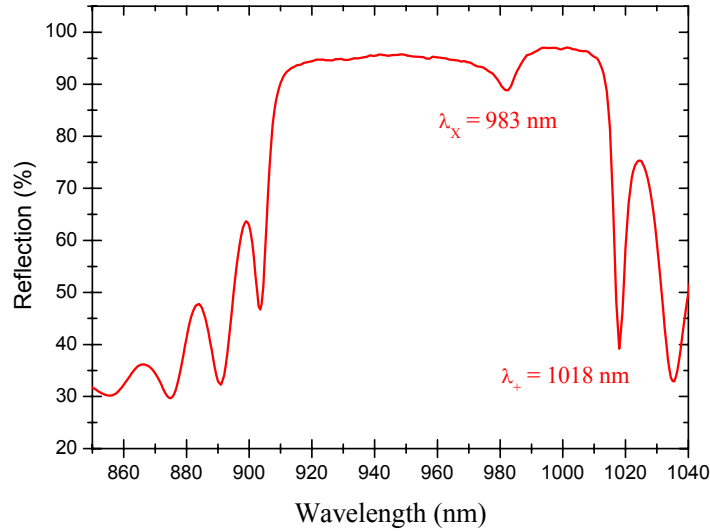


Figure 17 - Reflection spectrum from a second growth attempt at a QWDBR ODL structure. Here, a much more pronounced exciton absorption resonance ( $\lambda_x$ ) is evident (compare to Figure 13). In addition, this design puts  $\lambda_+$  at a shorter wavelength (1018 nm versus 1063 nm).

A dramatic illustration of how the improvements implemented on the GEN 2 MBE system have positively impacted device development is illustrated in Figure 17. This second generation device growth, like the first, was grown on an undoped GaAs substrate with a 2  $\mu\text{m}$  Si doped bottom GaAs buffer layer for n-metal contacting ( $n^+ \sim 2 \times 10^{18} \text{ cm}^{-3}$ ). This was followed by 31 periods of GaAs/AlAs DBR layers, again with 3 In(0.2)Ga(0.8)As quantum wells per GaAs layer. A final period included a top GaAs carbon-doped p+ cap layer ( $p^+ \sim 5 \times 10^{18}$ ) for the top p-Ohmic contact layer. Several features are clearly evident in this spectrum compared to that of Figure 13. First, there was a slight change in the design wavelength from  $\lambda_+ = 1064 \text{ nm}$  to  $\lambda_+ = 1018 \text{ nm}$ . This was done to accommodate the experimental true time

delay measurement capabilities of our UAH colleagues, as will be detailed later. Second, this figure also shows a much more prominent exciton absorption line, this time centered at 983 nm. Accordingly, we expected any changes resulting from the QCSE ( $\Delta n$ , or  $\Delta\alpha$ ) to result in much stronger effects on the long wavelength resonance at  $\lambda_+$ .

This second generation device was then processed in the same manner as the previous sample, with contacts applied and mounted in the transmission packaged designed for these experiments. We again tested the sample with low intensity broadband illumination in both transmission and reflection geometries to determine the influence of the QCSE on the long-wavelength bandedge resonance. Figure 18 shows the results of applying various strength electric fields to this device. Several features are evident from this graph. First, the character of the exciton absorption (as seen in the reflectivity spectrum) mimics closely the absorption spectrum of the MQW sample shown in Figure 11. Additionally, both the reflection and the transmission spectra show pronounced changes due to the QCSE at the desired positions, namely the long wavelength bandedge resonance,  $\lambda_+$ , near 1018 nm. These are strong indications of suitable QCSE influences, and warranted true time delay measurements by UAH.

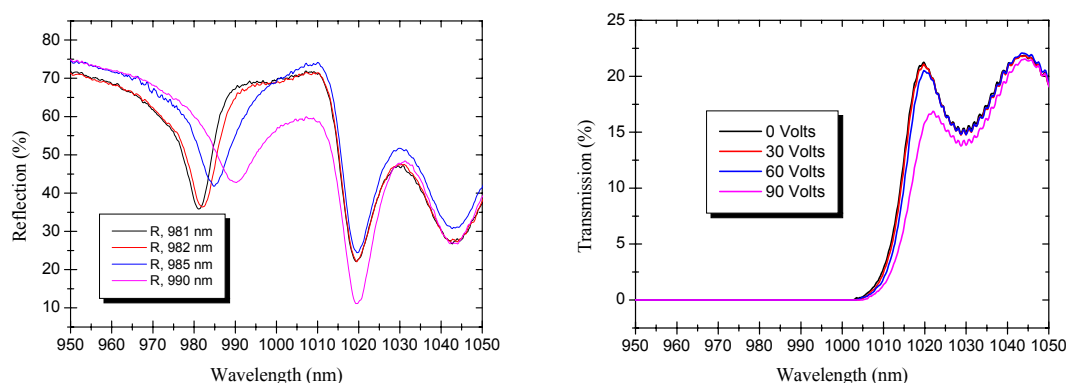


Figure 18 - Reflection spectrum (left) and Transmission spectrum (right) of G2-2544 with varying applied reverse bias. Note the similarity of the exciton absorption dip in the reflection spectrum to that of the absorption spectrum of the MQW sample shown in Figure 11. Both the reflection and transmission spectra show the influence of the QCSE at the bandedge resonance  $\lambda_+$ .

The static results shown in Figure 18 were good evidence of the soundness of our approach. What was truly required, however, was the ability to measure the true time delay (TTD) of a pulse propagating through the structure, and more importantly, the ability to measure the change in delay when an electric field is applied to our structure. Based on our simulations, we expected for this sample nominally 125 fs of *tunable* time delay for this structure. The most practical method to measure time delays on these ultrafast time scales is by means of an upconversion system utilizing a mode-locked laser. Ideally, one would like to use transform-limited pulses on the order of 1 ps time duration, such that the entire pulse duration fits within the wavelength span of the bandedge resonance. However, to measure these small tunable time delay changes, it is more practical to use femtosecond pulses for such an experiment.

At the start of this project, AFRL/MLP had such a laser in its possession, but did not have the expertise nor the additional optics and nonlinear crystals to perform an upconversion based true time delay measurement. Fortuitously, we were able to form a collaboration with

Professor Richard Fork at the University of Alabama in Huntsville to perform TTD measurements. Dr. Fork has a long history in ultrafast pulse generation and measurement systems [see e.g. 18], and was an early pioneer on the concept of super-continuum white light generation from such systems [19]. His group readily agreed to perform such measurements using equipment already at their disposal.

The experimental setup employed by UAH is depicted in Figure 19. A multi-line argon-ion laser is used to optically pump a mode-locked Ti:Sapphire, femtosecond laser. They divide the output pulse train (250 kHz pulse train of  $\sim 100$  fs pulses, with center wavelength of 810 nm) into a reference arm and a probe arm with a beamsplitter. A lens of focal length 75 mm focused the probe beam onto an optically flat sapphire crystal. This generated a white light continuum pulse train, spanning a spectral range from 400 – 1170 nm. The intensity of these continuum pulses falls rapidly near these limits, which provided the motivation for designing our second-generation sample at shorter wavelengths. A turning mirror directed the train of pulses in the reference arm to propagate nearly collinearly with the probe arm pulses. A lens of focal length 75 mm focused the beams to overlap spatially in a  $\beta$ -barium borate (BBO) nonlinear optical crystal. This crystal then serves to “upconvert” the two mixed arms to a higher energy signal in the visible. The output of this signal was then spatially isolated and focused onto the entrance slit of a spectrometer. A computer controlled translation stage varies the optical path length in the reference arm in a very precise fashion, such that the group delay between reference and probe pulses can be set over the temporal range of interest. By stepping

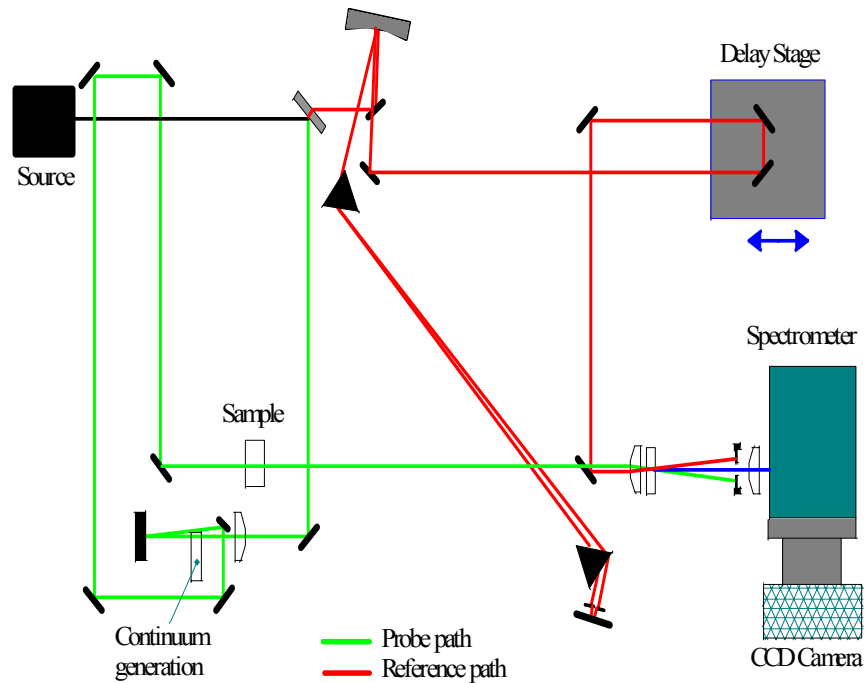


Figure 19 - Schematic of the true-time delay upconversion setup used by collaborators at the University of Alabama in Huntsville to characterize tunable delays in our QWDBR-ODL samples.

this translation stage, one then maps out the temporal evolution of the spectrum in 6.7 fs intervals (corresponding to fixed  $2 \mu\text{m}$  steps in the translation stage).

In the UAH setup, the continuum probe consisted of a family of pulses of 100 fs duration having an approximately uniform distribution (aside from a slight chirp) of



wavelengths over the region from 1000 to 1070 nm. While a variety of probes *could* be used, this particular probe was convenient given the 100 fs duration of the generating pulse. This family of pulses therefore provided information over three resonances beyond the photonic bandedge at  $\lambda_+$ . This served to tell us the effectiveness of these other resonances as potential ODL resonances arising from a single structure design.

Figure 20 presents two such TTD measurements. The first graph is simply a depiction of the pulse interfering with itself (“free space” delay), which serves to give a zero reference point for delay measurements. The second graph shows TTD from the empty DBR sample. This is the group delay produced by the combined DBR structure *and* the supporting 520  $\mu\text{m}$  thick GaAs substrate. Although this did not add significantly to the overall delay of the structure, the proximity of the bulk GaAs bandedge was such that it did contribute strongly to group velocity dispersion in these measurements. The UAH group devised a procedure to account for this dispersion and remove it numerically from the presented TTD measurement results. The measurements span a spectral region including the first three transmission peaks of the photonic band edge.

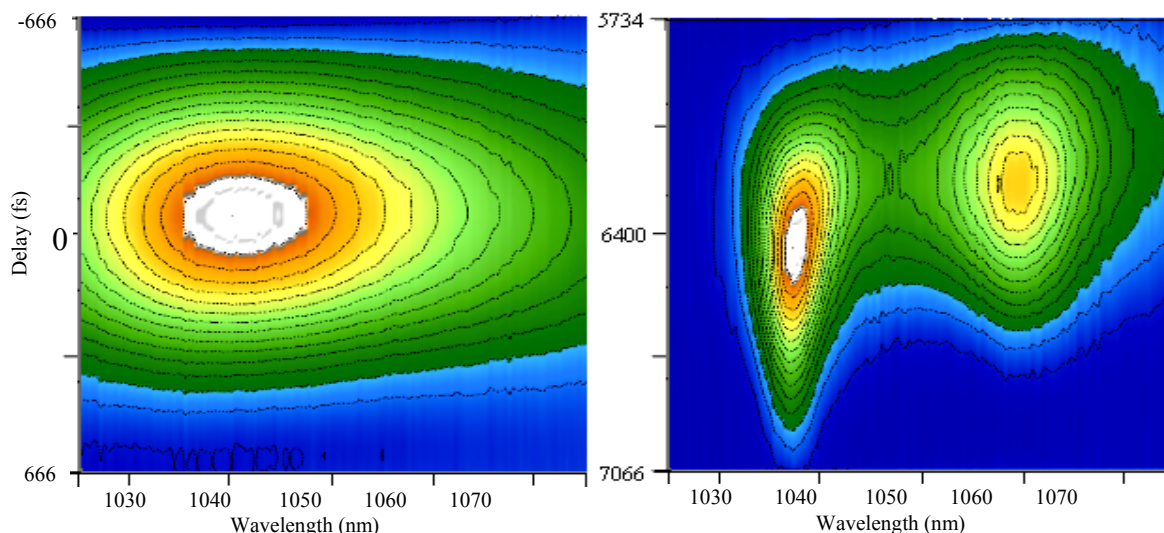


Figure 20 - Optical true-time delay measurements performed by UAH on (left) pulses propagating in free space (establishes a zero baseline in delay), and (b) from the first two long wavelength resonances of a 28 period DBR mirror structure.

As mentioned previously, the results shown in Figure 20 are simply static delay measurements, that is, a given structure would only yield a single fixed delay based on structure growth and relevant material parameters. However, with this measurement capability now in place, our next focus was on *tunable* TTD measurements from the QWDBR-ODL structure shown in Figures 17 and 18. Initial results were disastrous, but for obvious reasons. These QWDBR-ODL structures operate under relatively large electric field conditions ( $\sim 80$  kV/cm from the QCSE measurements of Figure 11). There is no intended current flow in the devices. In attempting to measure TTD changes with applied reverse bias, the original measurement system used white light continuum pulses in an attempt to capture nearly the complete device spectrum in a single shot, and then map out the temporal evolution of these



pulses by stepping the translation stage. Unfortunately, such broad pulses naturally gave rise to optical excitation of carriers (electrons and holes). The result of a sudden generation of quasi-free carriers under high electric field conditions was a rapid avalanche reverse breakdown of the devices. These effects either instantly evaporated the thin bonding wires leading to the device or, surviving this, would cause it to actually explode and leave a small crater in the wafer. Subsequent measurements, therefore, employed high-pass optical filters to spectrally narrow the spectrum of the probe arm pulses to a range  $\sim 1000$  nm to 1170 nm.

Figure 21 shows TTD measurements on our second QWDBR-OLD sample as a function of applied bias. Several conclusions can immediately be drawn from it. First and foremost, the amount of tunable delay for this sample over the safe operating range (0 to -100 V) was only  $\sim 25$  fs. This is a factor of 5x less than our predicted value of 125 fs. Furthermore, the QCSE influence falls off dramatically, as only the first resonance beyond the stopband shows any significant variation in time delay. Indeed, within this resonance itself, only a limited region exhibits the actual 25 fs amount of delay difference. Hence, we were looking at the maximal variation from this sample, and it was much less than predicted, let alone approaching the value of 1 picosecond required for multi-cycle time delay for beamsteering applications.

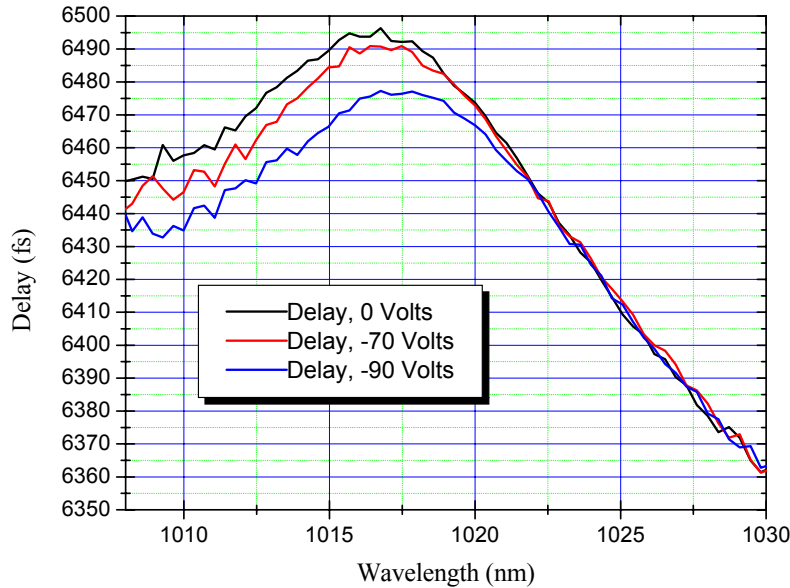


Figure 21 - Measured tunable TTD as a function of applied bias. These measurements were performed by UAH on the second generation QWDBR-ODL devices.

How do we account for the relatively weak performance in tunable delay from this purportedly much improved structure growth? Our first thought was that there existed a built-in electric field due to the presence of the doping layers, and that this field partially screened the QCSE from having its full influence. Simple dc testing of both the MQW and QWDBR-ODL samples, however, revealed that small forward biases (less than 1 V) were already sufficient to begin evidence of some forward current flow (limited by the heterostructure's

barrier potential). Hence, there was no reason to believe that significant Stark effect saturation due to these contact layers was responsible for this effect.

We have come to the conclusion that these poor results are an artifact of the measurement process itself inhibiting device performance. Recalling the results of Figure 4, which demonstrated that there is a resonant enhancement of the electric field amplitude in the QW containing GaAs layers of this structure, it is easy to see then that these high-energy, ultrafast pulses will also experience a strong resonant enhancement. Although the average power in this system is small, the instantaneous fields generated in the structure can be quite intense. This should have been intuitive given the nature of the measurement technique—upconversion in a nonlinear crystal via intense two-field mixing. Ideally, one would like to take the probe arm power to as small a value as possible, but doing this caused a significant drop in the upconverted signal, severely degrading signal to noise and rendering results useless. Hence, we are in the unfortunate position of having demonstrated poor performance without disproving the concept of the methodology.

## **V. Conclusions and Suggestions for Further Study**

Our goal in this effort was the development of monolithic, electrically tunable optical delay lines for true time delay applications. An intended result of this work was a monolithic device structure that could be incorporated with one- or two-dimensional arrays of VCSELs for use in generating phased arrays of such laser diodes. Multi-cycle delays would be required for any practically useful system (non-negligible beamsteering angles), which meant true time delay devices capable of delivering delays on the order of 1 picosecond. We were able with our QWDBR-ODL approach to only generate delays on the order of 25 fs using the straightforward approach taken, namely implementing isolated quantum wells within a traditional DBR structure. Although this was a novel result, it was much less than the anticipated results of 125 fs of tunable delay.

How might a future effort in this arena be improved? Our explanation of why the device performed less than ideally would first require further investigation. If one could more asymmetrically divide the probe and reference pulses in the TTD setup of figure 19, then an even weaker probe beam could be used within the sample. This could eliminate self-saturation of the effect, and validate quantitatively the soundness of our approach. Unfortunately, time and budget limitations, as well as other research priorities by our collaborators, forced us to abandon this route.

Another possible means of improvement is to enhance the amount of index change arising from the QCSE itself. At the time of this research, groups were interested in the effects of asymmetric coupled quantum wells for electro-absorption modulators [20]. These structures were primarily AlGaAs based waveguide structures (Mach-Zehnder modulator devices), but the concept could be generalized to our devices. We explored some variations of this theme with the FEM bandstructure code of Ram-Mohan [15]. At that time, we had only the full material parameters for the AlGaAs system, and needed strain-inclusive simulation capability for InGaAs materials (to stay below the GaAs bandgap). Nevertheless, we did perform a series of simulations to attempt to verify the usefulness of this approach (see Figure 22). In this simulation, three GaAs wells of varying widths are used, leading to three different sets of

energy levels. By inserting thin AlGaAs barriers between the wells, we couple their levels, resulting in a shifted (split through coupling) energy spectrum. This figure shows the wavefunctions of the ground state and the first excited state of an asymmetric coupled three well system under zero field (left), and under 10 kV/cm applied field (right). What is significant to note is that the wavefunctions almost completely localize into one well or the other under these relatively small fields (recall from Figure 11 that fields of nearly 100 kV/cm were required to quench the excitons in the isolated well system). Indeed, such a sample could be grown in the GEN 2 MBE system, and this index and absorption behavior studied. However, since this is for AlGaAs material only, one would have to take special processing steps to thin/remove the absorbing GaAs substrate in order to validate this design. Most researchers have investigated this phenomenon by launching light in a waveguide parallel to the plane of the wafer. We, however, are interested in the direction perpendicular to the wells. As the QCSE is not homogeneous in direction ( $k_{\perp}$  not equivalent to  $k_{\parallel}$ ); hence, this structure is not directly applicable our investigations. Since the time of this ODL research, we have added full strain-inclusive bandstructure parameters that would allow us to work in an InGaAs/GaAs system, applicable to this effort. Such designs could lead to significant device improvement.

Another area of investigation that was conjointly pursued for improved monolithic ODL device design was attempts to shed the simple DBR approach, and investigate other novel, perhaps aperiodic structures. Among some of the concepts pursued from a simulation standpoint included growing layers in Fibonacci type sequences, and even arranging structures such that the layers formed a pattern following the Golden Mean. As a general rule, however, all of these structures showed performance similar to the simple DBR structure, namely that enhanced delay was accompanied by a dramatic sharpening of the transmission resonance, thereby reducing the application of such a structure in any practical system. In

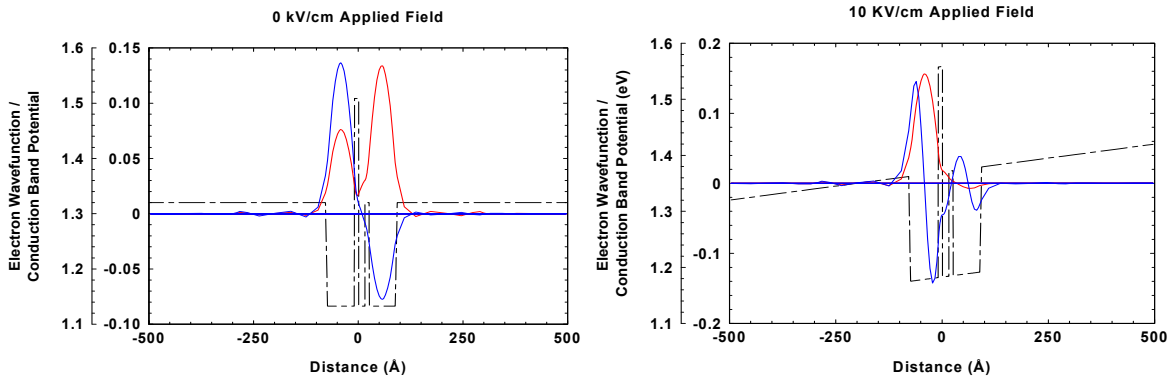


Figure 22 - Ground state (red) and first excited state (blue) wavefunctions for an asymmetric coupled quantum well system. Here, three GaAs QWs are separated by 2 AlGaAs barrier (and terminating AlGaAs barrier material). Application of a 10 kV/cm electric field serves to strongly localize these states.

investigation of aperiodic structures, it quickly became apparent that unless we appealed to application of genetic algorithms and the use of constrained optimization techniques (maximum group velocity change while maintaining a minimum pulse distortion in a “growable” device structure), it would be nearly hopeless to expect to simply stumble upon a device structure that would show any significant improvement over the aforementioned designs.

One tangential area of investigation that did prove fruitful was the investigation of a static phase modulator [21]. This resulted from an expansion of our collaboration with the group at UAH, in particular, Andrew Keys. Phase modulator specifications derived from the end goal of arraying multiple individually controllable modulating elements at wavelength spacings in one- or two-dimensional transmissive arrays for use in optical signal beam steering applications. We sought a modulator design possessing a bandpass region of high average transmission, capable of providing continuous, controllable, and reconfigurable relative phase modulation for a selected signal bandwidth of optical frequencies. We desired in this effort that the selected signal bandwidth as the minimum spectral range of contiguous wavelengths required to describe a transform-limited optical signal pulse in terms of its root mean square (RMS) spectral width. Hence, we defined the modulator's bandpass region as being at least *twice* the minimum range of contiguous wavelengths required to fully transmit the entire optical signal bandwidth. We chose this bandpass region width to allow ample spectral bandwidth for a full cycle phase modulation of the signal's frequency components without edging components out of the bandpass region. We further required that the bandpass region maintain a relatively consistent level of transmission to ensure all optical signal frequency components are transmitted with even amplitude. The transmitted phase profile within the bandpass region is specified to change from 0 to  $4\pi$  as measured in relative terms from one edge of the bandpass to the other. This provided a consistent phase modulation of all optical signal frequencies within the predetermined optical signal bandwidth. We further desired that the rate with which the transmitted phase changes with respect to frequency to be a near-linear function, reducing the level of phase distortions introduced to the propagating optical signal, such as group velocity dispersion and other higher order distortions that contribute to pulse spreading and frequency chirping.

To meet these bandpass modulator design specifications, we employed recent advances in optical interference coating design to engineer a computationally optimized bandpass configuration. The design process for our particular implementation of the bandpass modulator began with an initial bandpass filter design as described by the expression

$$S | HLHLHLHLH (11H LHLHLHLHLHL 11H)^5 3H | A$$

where  $S$  represents the interface to the stack substrate,  $L$  represents a material layer with a relatively low refractive index value and an optical thickness of  $\lambda_0/4n_L$ ,  $H$  represents a material layer with a relatively high refractive index value and an optical thickness of  $\lambda_0/4n_H$ , and  $A$  represents the air interface. We chose AlAs as the material possessing a relatively low refractive index value and GaAs as the material possessing a relatively high refractive index value. Exponential notation in the above "equation" implies a repeating period of layers. The entire structure is then intended to be grown on a GaAs substrate. For the initial design, we choose 1000 nm for  $\lambda_0$ , which centered the high-transmission bandpass region on this near-infrared wavelength.

We used the transfer matrix technique to obtain the wavelength-dependent complex transmission coefficient for the multilayered stack configurations. Our models accounted for material dispersion through formulae describing the wavelength-dependent refractive indices of GaAs and AlAs. We used the convention that the optical signal enters the structure from the substrate side, passes through the multilayered stack, and exits into air. When modeling the

initial configuration, we found that the initial bandpass modulator design had a transmission bandpass region with the transmission level ranging between 93.00 and 100.00 percent (not accounting for the initial reflection of signal when passing the air/substrate interface). Computational optimization further reduced the rippling peak-to-valley variations of the transmission region. We employed an optimization technique, referred to as “needling,”[22] to strategically insert 10 nm thick layers of AlAs within specific layers of GaAs at computationally-prescribed locations such that the average transmission level across the width of the bandpass is improved. This incremental optimization process resulted in a much smoother transmission bandpass function. The “post-needling” transmission level of the final bandpass configuration ranged between 96.85 and 100.00 percent. The optimization process converted the initial bandpass configuration of 79 layers into a final configuration of 91 layers by splitting six layers of GaAs with thin layers of AlAs. Assessment of the phase component of the complex transmission coefficient showed that the final bandpass modulator configuration exhibited the specified, near-uniform, transmitted relative phase change as measured across the transmission bandpass region. The bandpass region exhibited a spectral width 21 nm, or by the differential relationship of  $d\nu = |(c/\lambda^2)d\lambda|$ , 6.3 THz at a wavelength of 1000 nm. We emphasize that this computationally improved design is not necessarily globally optimal, but it did improve the average transmission level of the bandpass modulator and exhibited the specified transmitted phase characteristics. A detailed layer-by-layer description of the final bandpass modulator configuration is provided in the Table 1.

We found through our simulations that a 1.3 percent reduction in refractive index values for all GaAs and AlAs layers would give rise to full cycle phase modulation for the defined optical signal bandwidth. Final implementation of such a tunable bandpass modulator would then seek to implement a nonmechanical method for producing this refractive index change. However, for this proof-of-concept experiment, we employed angle of incidence modulation to alter the optical path lengths experienced by the propagating optical signal. As the angle of incidence is increased, the optical thickness of the layers increases in a fashion that is inversely proportional to the angle’s cosine. An increase in the angle of signal incidence provided an approximation to the effects resultant from a uniform change in refractive index throughout the stack’s layered materials.

The design outlined in Table 1 was then grown by molecular beam epitaxy (MBE) at AFRL. The finished sample was then cleaved into four quarters for use in experimental characterization. Figure 23 shows the reflectivity spectrum of the resultant sample.

Layer Number	Thickness (nm)	Material	Layer Number	Thickness (nm)	Material	Layer Number	Thickness (nm)	Material
Substrate		GaAs	31	71.67	GaAs	62	10.00	AlAs
1	30.00	GaAs	32	84.82	AlAs	63	51.67	GaAs
2	10.00	AlAs	33	71.67	GaAs	64	84.82	AlAs
3	31.67	GaAs	34	84.82	AlAs	65	71.67	GaAs
4	84.82	AlAs	35	71.67	GaAs	66	84.82	AlAs
5	71.67	GaAs	36	84.82	AlAs	67	71.67	GaAs
6	84.82	AlAs	37	71.67	GaAs	68	84.82	AlAs
7	71.67	GaAs	38	84.82	AlAs	69	71.67	GaAs

8	84.82	AlAs	39	71.67	GaAs	70	84.82	AlAs
9	71.67	GaAs	40	84.82	AlAs	71	71.67	GaAs
10	84.82	AlAs	41	71.67	GaAs	72	84.82	AlAs
11	510.00	GaAs	42	84.82	AlAs	73	71.67	GaAs
12	10.00	AlAs	43	1480.00	GaAs	74	84.82	AlAs
13	340.09	GaAs	44	10.00	AlAs	75	1576.84	GaAs
14	84.82	AlAs	45	86.84	GaAs	76	84.82	AlAs
15	71.67	GaAs	46	84.82	AlAs	77	71.67	GaAs
16	84.82	AlAs	47	71.67	GaAs	78	84.82	AlAs
17	71.67	GaAs	48	84.82	AlAs	79	71.67	GaAs
18	84.82	AlAs	49	71.67	GaAs	80	84.82	AlAs
19	71.67	GaAs	50	84.82	AlAs	81	30.00	GaAs
20	84.82	AlAs	51	71.67	GaAs	82	10.00	AlAs
21	71.67	GaAs	52	84.82	AlAs	83	31.67	GaAs
22	84.82	AlAs	53	71.67	GaAs	84	84.82	AlAs
23	40.00	GaAs	54	84.82	AlAs	85	71.67	GaAs
24	10.00	AlAs	55	71.67	GaAs	86	84.82	AlAs
25	21.67	GaAs	56	84.82	AlAs	87	71.60	GaAs
26	84.82	AlAs	57	71.67	GaAs	88	84.82	AlAs
27	71.67	GaAs	58	84.82	AlAs	89	71.67	GaAs
28	84.82	AlAs	59	1576.84	GaAs	90	84.82	AlAs
29	1576.84	GaAs	60	84.82	AlAs	91	1003.44	GaAs
30	84.82	AlAs	61	10.00	GaAs	Air Interface		Air

Table 1 - Detailed design parameters of the transmission phase modulator [20].

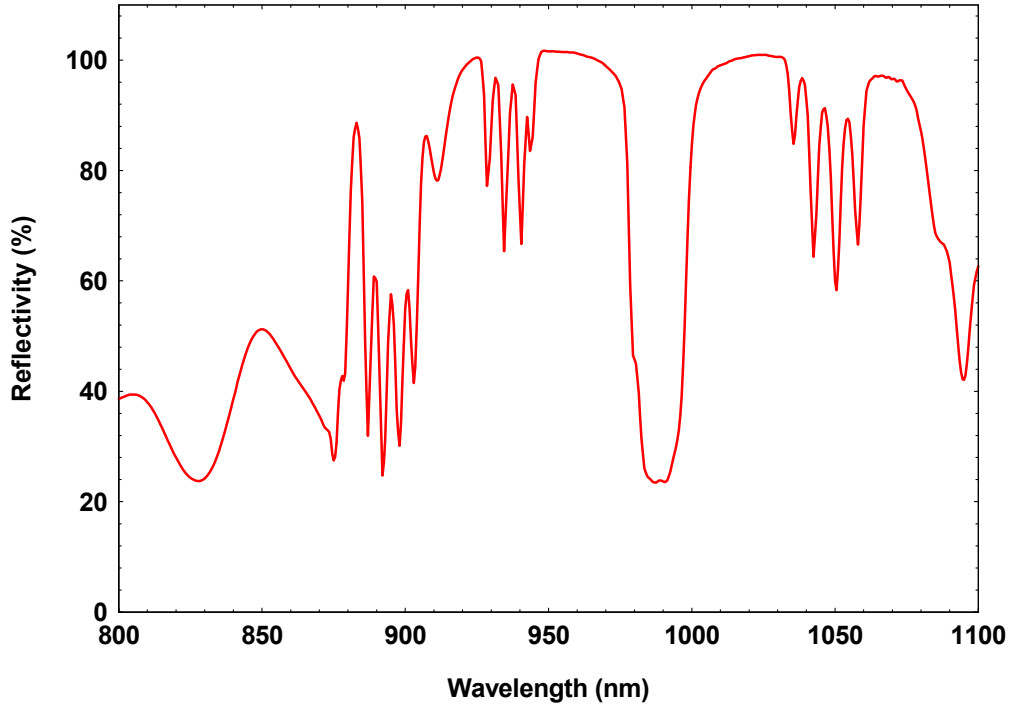


Figure 23 - Reflection spectrum for the MBE-grown Phase Modulator sample design of Table 1.

Our technique for separating the bandpass modulator's contribution to the measured phase profile from the total sample's measured phase profile required the measurement of the phase as transmitted through *only* the substrate. Therefore, we plasma etched a 5 mm "hole" in the sample, removing the multi-layered epitaxial growth and exposing the substrate to an air interface. We etched the hole by coating the sample with an appropriate resist, then removed the structure using an inductively coupled plasma reactive ion etching system. Our laser reflectance measurement system provided real-time monitoring of the etch process, and allowed us an accurate method for determining when the bandpass multilayer structure was completely etched away from the substrate.

Characteristic of the molecular beam epitaxy growth process, the sample's layers exhibited a radially-dependent parabolic decrease in thickness across the sample's surface. Figure 24 shows a spectral image of the sample's transmission as measured by the spectrometer's input slit when oriented in a radial direction relative to the sample. The etched hole region is intentionally positioned to illuminate the center portion of the spectrometer's input slit. The decrease in layer thickness is evident in the top and bottom sections of the spectrometer output image. While the etched hole region exhibits full transmission across the imaged spectrum, the transmission bandpass drifts from longer to shorter wavelengths in accordance with the location of measurement as made by the radially-oriented spectrometer slit. We measured all bandpass transmission and phase profiles as transmitted by an area near the sample's radial center. Here, the specified central wavelength of the bandpass region, designed for 1000 nm, turned out to be 989 nm (see Figure 23 above). This difference may be attributable to slight growth rate instabilities on behalf of the MBE process. Measurements of the transmission bandpass made at other sample locations are all centered at shorter wavelengths than 989 nm, confirming the radially-dependent fall-off in layer thickness. We

ran computational predictions of the transmission and phase profiles to compared against the measured values. When conducting these new predictions, we replaced the original design wavelength of 1000 nm with the measured wavelength of 989 nm, which provided an accurate prediction of the physical sample's complex transmission coefficient. types of measurements: the spectral transmission profile of the bandpass modulator versus angle of incidence ( $\theta$ ), and the spectral transmitted relative phase profile versus angle of incidence. These measurements are compared to predicted values for the transmission and phase and are plotted below.

As a demonstration of the ability of the bandpass structure to act as a phase modulator, we used an optical signal with a Gaussian envelope, a center wavelength of 984.8 nm, and a root-mean-square width of 5 nm, corresponding to a pulse length of 52 fs. Selection of these parameters intentionally positioned the signal's rms bandwidth within the shorter half of the unmodulated bandpass region. The accompanying figures clearly mark the signal's spectral bandwidth position and its relation to the spectral transmission and phase profiles.

The source used in taking the measurements was broadband rather than narrowband to illuminate the entire spectral region of interest with a relatively uniform level of illumination. We employed a 200 W Quartz-Tungsten-Halogen (QTH) lamp as the primary source of

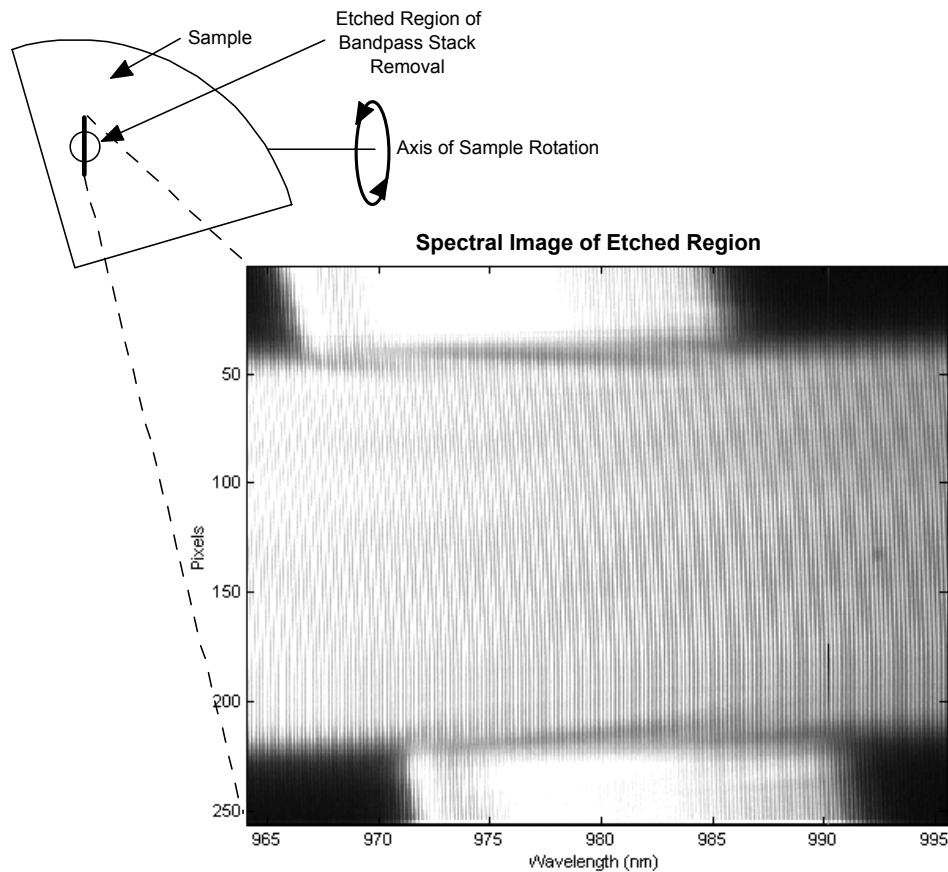


Figure 24 - Spectral image depicting interference functions of both the transmission bandpass region and the “etched hole” region of the sample being experimentally characterized.



The experimental characterization of the bandpass modulator comprised two primary illumination during the experimental measurement process. We measured the spectral profiles of both transmission and phase using a half-meter spectrometer and holographic grating optimized to wavelengths near 900 nm. A computer-controlled, liquid nitrogen-cooled CCD camera recorded the spectral output of all transmission and phase measurements.

We obtained the transmission profile of the bandpass modulator by placing the sample directly in front of the spectrometer slit and illuminated it with the broadband QTH source. A spectral sweep ranging from 900 nm (the region in which GaAs transitions from opaque to transparent) to 1100 nm allowed the spectrometer to record the transmission profile of the bandpass modulator. The measured and predicted transmission spectra for four different angles of incidence are depicted in Figure 25. When comparing the predicted values to the measured data, we accounted for the initial air to substrate reflection losses, reducing the transmission from 100% to about 60%.

The angular dependence of the bandpass region's spectral position is indicated in the figure as data was taken at ten degree increments from zero to thirty degrees.

A detailed examination of the normalized transmission spectrum revealed the transmission spectrum appears to be modulated by a high-frequency oscillation. This phenomenon was particularly prominent in the transmission profile plot corresponding to an angle of incidence of zero degrees. The oscillation was a consequence of the sample acting as a resonator for optical signals propagating through the substrate/stack combination. The free spectral range of these oscillations revealed a combined substrate and sample thickness of about 760  $\mu\text{m}$ .

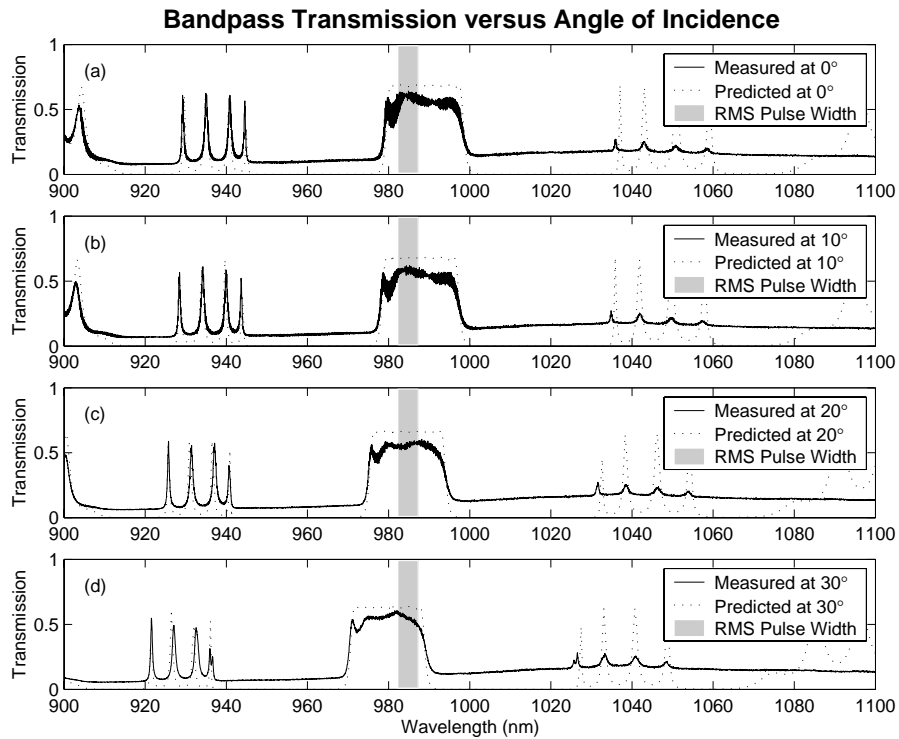


Figure 25 - Plot of predicted and experimentally measured bandpass modulator transmission profiles at (a) normal incidence to the sample, (b) ten degree angle of incidence, (c) twenty degree angle of incidence, and (d) thirty degree angle of incidence.

The absolute phase of an optical signal is difficult to measure experimentally as it rapidly accumulates within relatively small distances. It is much more convenient to measure phase in relative terms rather than absolute terms. An interferometer provided the means for making relative phase measurements in this investigation. By splitting a single optical beam into two halves, one half is used to probe the sample and the other half to act as the phase reference beam. The interferometer then recombined each half, revealing the wavelength-dependent variations in intensity used to discern the relative phase difference existing between the wavefronts of each of the two beam halves.

The UAH group used a modified Mach-Zehnder interferometer configuration as depicted schematically in Figure 26. One leg of the interferometer contained the sample mounted to a rotating holder so that either the bandpass region or the etched region may be positioned for analysis by the spectrometer. The other interferometer leg contained no sample elements, but rather had mirrors mounted on a translatable linear motion stage. The translation stage provided a means of implementing phase-stepping interferometry techniques [23] to map out relative phase versus angle of incidence.

The measured relative transmitted phase profiles versus the predicted relative transmitted phase profiles for four different angles of incidence are depicted in Figure 27. The angular dependence of the bandpass region's spectral position and the rms bandwidth for an optical signal propagating through the modulator are indicated in the figure as data was taken at ten degree increments from zero to thirty degrees.

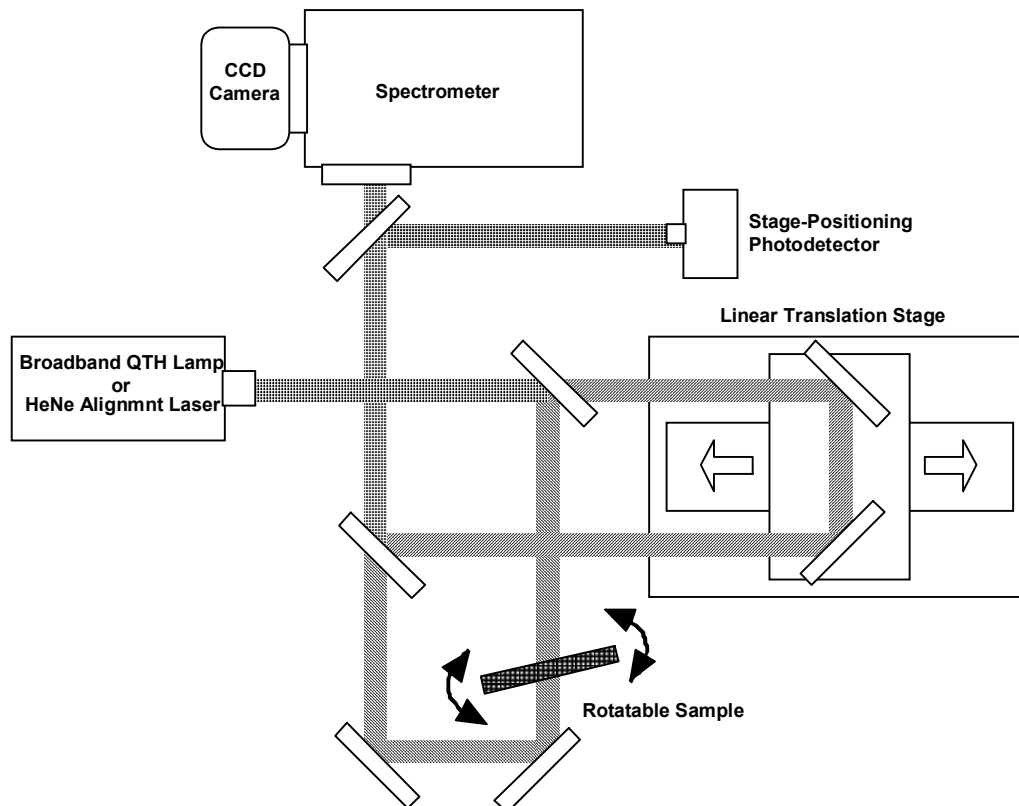


Figure 26 - Diagram of modified Mach-Zehnder interferometer used to characterize the bandpass modulator's transmitted phase profile versus wavelength.

From Figure 27, we observed close agreement between predicted values and measured data for the transmitted relative phase, but only within the indicated transmission bandpass for each of the four angles of incidence. We further noticed a rapid departure of the measured data from predicted values for wavelengths outside of the indicated transmission bandpass. This discrepancy is an artifact of the measured difference between phase as transmitted by the substrate and phase as transmitted by the total sample; it does not accurately report the transmitted phase in this region. At wavelengths outside of the transmission bandpass, the modulator is opaque, providing no phase data. In other words, the transmitted phase of the substrate accumulates without restraint from the total sample measurement, giving the false indication that the transmitted phase is rapidly changing in this region. We considered blanking this data from the measured plots of transmitted phase by reasoning that phase information outside of the transmission bandpass is irrelevant. However, we found it instructional to the nature of the measurement technique, so the data is therefore fully presented in Figure 27.

The transmitted phase modulation profile represents the difference between a reference transmitted phase and a modulated transmitted phase. We define the reference transmitted phase as that transmitted phase profile incurred by a propagating optical signal as it traverses the bandpass modulator at normal incidence. We next define the modulated transmitted phase as that phase profile incurred by a propagating optical signal as it traverses the bandpass modulator at some angle of incidence other than normal incidence. Figure 28 shows the transmitted phase modulation versus wavelength for a ten degree, a twenty degree, and a thirty degree angle of incidence. Predictions of the transmitted phase modulation are also included in the plots.

Plots of the transmitted phase modulation at increasing angles of incidence indicate the trend of a growing difference between predicted values and measured data as assessed at the defined optical signal's center wavelength of 984.8 nm. For example, at a thirty degree angle of incidence, we predicted the transmitted phase modulation of 5.27 radians and measure a transmitted phase modulation of 4.08 radians for a difference of 1.19 radians. We attributed this discrepancy to subtle differences between the parameters used in simulating the multilayered stack and the physical parameters actually comprising the layers, including variations in physical layer thickness, substrate thickness, and GaAs and AlAs refractive index values. We again observed a departure of measured data from predicted values for wavelengths outside of the transmission bandpass. This difference, like the difference observed in the relative transmitted phase plots, is attributed to the lack of phase data outside of the modulator's bandpass region due to its opacity.

Again, the phase change has been tuned mechanically by tilting the sample with respect to the path of the beam. However, in noticing the design of the structure, there are sections of the design calling for 11 periods of high index ("H", or GaAs) material layers, and this is repeated 5 times in this design without detrimental influence on the pulse bandwidth. In a electrically tuned device, one could envision utilizing a similar structure, but now incorporating  $\text{In}(x)\text{Ga}(1-x)\text{As}$  quantum wells of a prescribed alloy composition and well width to index tune the structure via the QCSE. In this case, there would be more leverage for placement of the wells relative to the region of high transmission, and effects would be more easily measured.

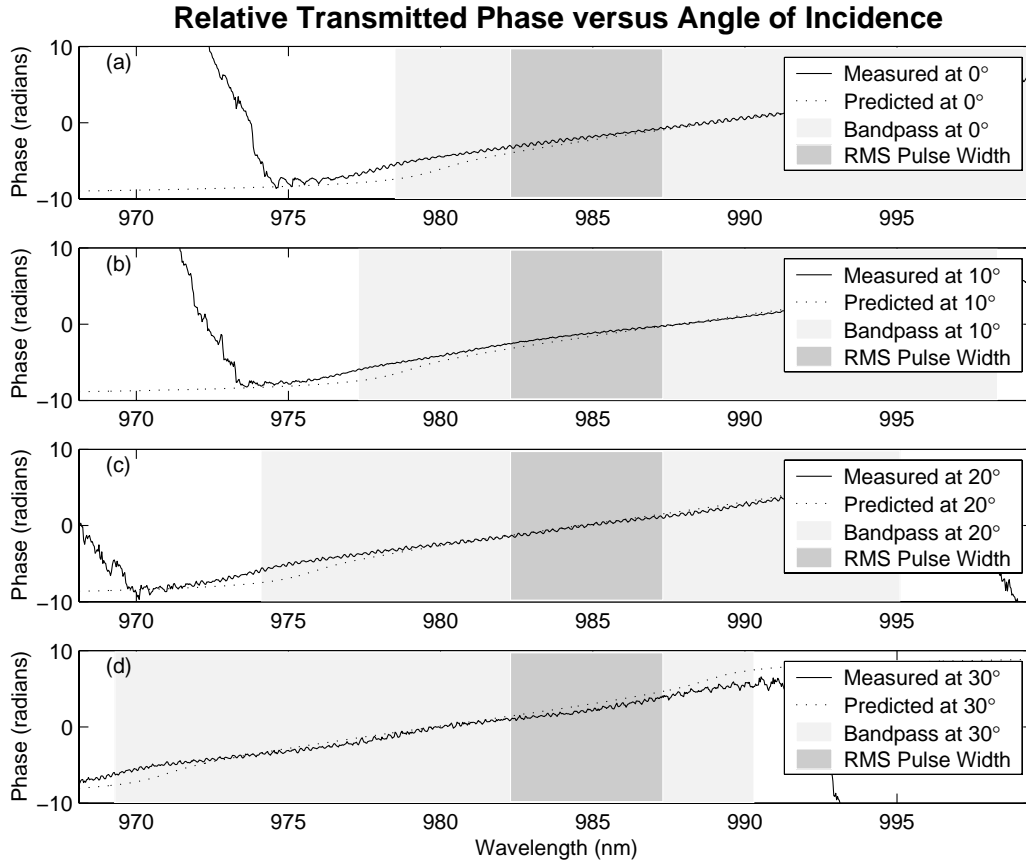


Figure 27 - Plot of predicted and experimentally measured relative phase profiles as transmitted within the modulator's bandpass region at (a) normal incidence to the sample, (b) ten degree angle of incidence, (c) twenty degree angle of incidence, and (d) thirty degree angle of incidence.

Finally, another possible method for improved device performance suitable for an air-based platform could be realized through a combination of the phase modulator concept acting in conjunction with micro-electro-mechanical system (MEMS) tunable structures. As a concept, we illustrate in Figure 29 recent efforts toward development of hybrid MEMS tunable lasers and filters for optoelectronics applications [24]. This figure shows the concept of flip-chip bonding a III-V mirror or laser onto a foundry (such as MUMPS or SUMMIT) MEMS tunable cantilever structure. In this concept, the MEMS flexure is electrostatically controlled to move up and down through application of an applied bias. A III-V structure such as a VCSEL (tunable laser) or DBR mirror (tunable filter) is then flip-chip bonded onto the flexure.

By using a coupled cavity approach, one is able to tune the coupled-cavity resonance in wavelength space.

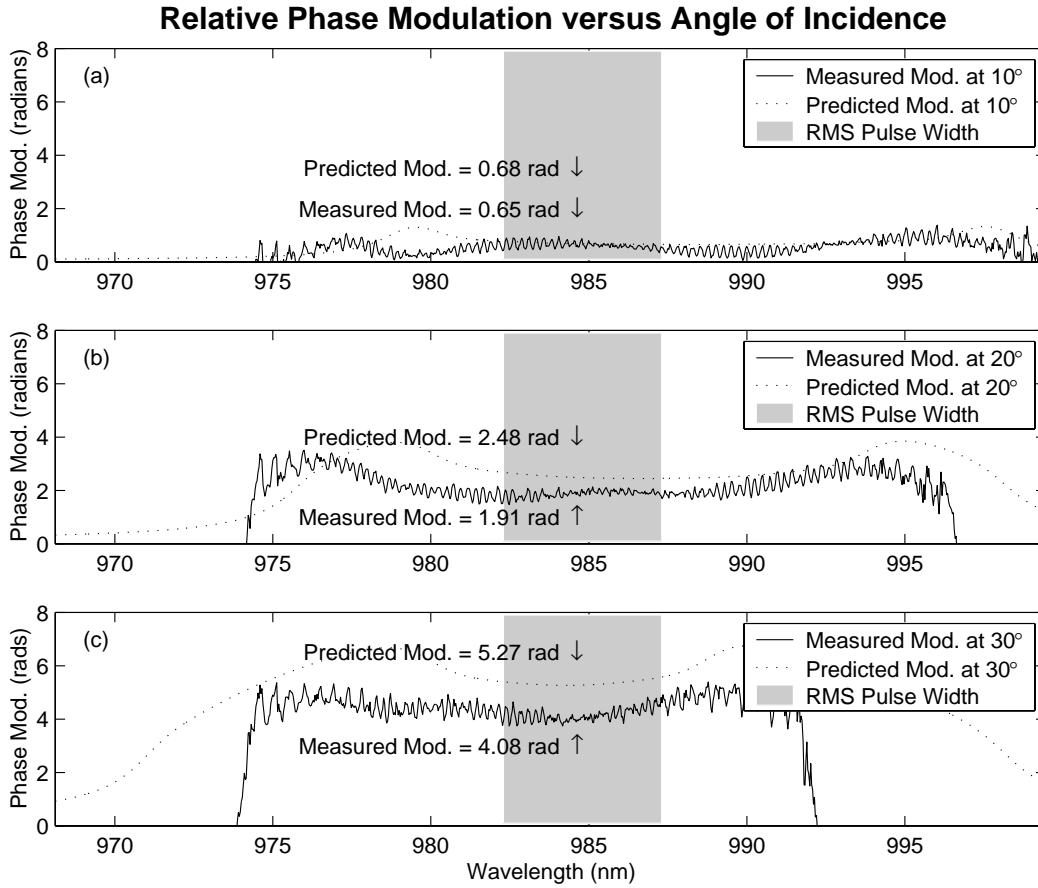


Figure 28 – Plot of predicted and experimentally measured relative phase modulation profiles represented by the difference between the transmitted relative phase at normal incidence to the sample and the transmitted relative phase at (a) ten degree angle of incidence, (b) twenty degree angle of incidence, and (c) thirty degree angle of incidence.

Traditionally this type of device has been used for wavelength tuning applications by physically altering the optical path length via changing an air-gap in the structure. Use of these type of structures as phase modulators or optical delay lines, however, has heretofore been largely unexplored. As a resonant device, changes in path length (and hence phase or delay changes) are enhanced through multiple reflections and constructive phase interference. By judiciously designing the combination of MEMS device and flip-bonded structure—as in our transmissive phase modulator construction—one could conceivably have very low loss delay lines with relatively broad transmission bandwidths. Progress and time warranting, we will likely investigate this concept in conjunction with collaborators for measurements on such structures.



- [8] Fan, L., M.C. Wu, and K.D. Choquette, "Two-dimensional scanning microlenses for vertical-cavity surface-emitting lasers," *Proc. Conference on Lasers and Electro-Optics (CLEO)* '97, p. 19 (1997).
- [9] see for example Levandovsky, D., M. Vasilyev, and P. Kumar, "Near noiseless amplification of light by a phase-sensitive fibre amplifier," *Pramana J. of Physics* **56** (2-3), pp. 281-285, 2001.
- [10] Miller, D. A. B., D. S. Chemla, T. C. Damen, A. C. Gossard, W. Wiegmann, T. H. Wood, and C. A. Burrus, "Electric field dependence of optical absorption near the band gap of quantum-well structures," *Phys. Rev.* **B 32**, 1043 (1985).
- [11] Blum, O., J. E. Zucker, T. H. Chiu, M. D. Divino, K. L. Jones, S. N. G. Chu, and T. K. Gustafson, "InGaAs/InP multiple quantum well tunable Bragg reflector," *Appl. Phys. Lett.* **59**, 2971 (1991).
- [12] Blum, O., J. E. Zucker, X. Wu, K. H. Gulden, H. Sohn, T. K. Gustafson, and J. S. Smith, "Low-voltage-tunable distributed Bragg reflector using InGaAs/GaAs quantum wells," *IEEE Phot. Tech. Lett.* **5**, 695 (1993).
- [13] Kavaliauskas, J., G. Krivaite, A. Galickas, I. Šimkiene, U. Olin, and M. Ottosson, "Quantum confined Stark effect in InGaAs/GaAs quantum wells under high electric fields," *Phys. Stat. Sol. (B)* **191**, 155 (1995).
- [14] Di Dio, M., M. Lomascolo, A. Passaseo, C. Gerardi, C. Giannini, A. Quirini, L. Tapfer, P. V. Giugno, M. De Vittorio, D. Greco, A. L. Convertino, L. Vasanelli, R. Rinaldi, and R. Cingolani, "Structural and optical studies of  $\text{In}_x\text{Ga}_{1-x}\text{As}/\text{GaAs}$  multiple quantum wells," *J. Appl. Phys.* **80**, 482 (1996).
- [15] **Finite Element and Boundary Element Applications in Quantum Mechanics**, L. R. Ram-Mohan, Oxford University Press, September, 2002.
- [16] See, for example, "Influence of Structural Disorder and Light Coupling on the Excitonic Response of Semiconductor Microcavities," C. Ell, J. Prineas, T.R. Nelson, Jr., S. Park, H.M. Gibbs, G. Khitrova, S.W. Koch, and R. Houdré, *Phys. Rev. Lett.* **80** (21), 4795-4798 (1998).
- [17] Unaxis Incorporated, St. Petersburg, Florida, 33716, private communication.
- [18] Gamble, L.J., W.M. Duffey, S.T. Cole, R.L. Fork, D.K. Jones, T.R. Nelson, Jr., J.P. Loehr, J.E. Ehret, "Simultaneous Measurement of Group Delay and Transmission of a One-Dimensional Photonic Crystal," *Optics Express* **5**, 267-272 (1999).
- [19] R.L. Fork, C.V. Shank, C. Hirlmann, and R. Yen, "Femtosecond white-light continuum pulses," *Optics Letters* **8** (1), p. 1. (1983).

- [20] See, for example, H. Feng, M. Sugiyama, K. Tada, and Y. Nakano, "Field Induced Optical Effect in a Five-Step Asymmetric Coupled Quantum Well with Modified Potential," *IEEE Journ. of Quant. Electr.* **34**, pp. 1197-1208 (1998).
- [21] Keys, A.S., R.L. Fork, T.R. Nelson, Jr., J.E. Ehret, and J.V. Van Nostrand, "Characterization of a multi-layered dielectric transmissive phase modulator," *Technical Digest for SPIE's 46<sup>th</sup> Annual Meeting, Conference 4438, Physics, Theory, and Applications of Periodic Structures in Optics*.
- [22] Tikhonravov, A.V., M. K. Trubetskov, and G. W. DeBell, "Application of the needle optimization technique to the design of optical coatings," *Applied Optics*, **35**(28), pp. 5493-5508, 1996.
- [23] See, for example, P. Hariharan, **Basics of Interferometry**, Appendix L, Academic Press, Inc., Harcourt Brace Jovanovich, Boston, 1992.
- [24] Ochoa, E.M., L.A. Starman, Jr., W.D. Cowan, T.R. Nelson, Jr., O. Blum Spahn, and J.A. Lott, "**Polysilicon prototypes for flip-bonded hybrid MEM-tunable filters and VCSELs**," *Fifth International Conference on Modeling and Simulation of Microsystems*, April 22-25, 2002, San Juan, Puerto Rico, USA.